QUANTITATIVE *IN VIVO* DRUG DELIVERY RESEARCH USING MAGNETIC RESONANCE

by

Xin Liu

A dissertation submitted to the faculty of
The University of Utah
in partial fulfillment of the requirements for the degree of

Doctor of Philosophy

in

Physics

Department of Physics and Astronomy

The University of Utah

December 2011

Copyright © Xin Liu 2011

All Rights Reserved

The University of Utah Graduate School

STATEMENT OF DISSERTATION APPROVAL

The dissertation of **Xin Liu**

has been approved by the following supervisory committee members:

Brian Saam	, Chair	**06/17/2011** Date Approved
Eun-Kee Jeong	, Member	**06/17/2011** Date Approved
Dennis Parker	, Member	**06/17/2011** Date Approved
Eugene Mishchenko	, Member	**06/17/2011** Date Approved
Gernot Laicher	, Member	**06/17/2011** Date Approved

and by **David Kieda**, Chair of the Department of **Physics and Astronomy**

and by Charles A. Wight, Dean of The Graduate School.

ABSTRACT

Over the past decade, molecular imaging has emerged as a powerful tool to visualize biological processes of living subjects on the cellular or molecular level. Such techniques greatly improve our understanding of disease and drug activity. Since molecular imaging relies on exoteric imaging agents as reporters to send detectable signals towards the outside, investigation of the imaging agents is of vital importance. However, the quantification of the imaging agents is still one of the challenges facing this work.

Magnetic resonance (MR) imaging has been widely used as one of the imaging modalities for molecular imaging. This dissertation focuses on the quantification of the gadolinium based contrast agent (GBCA) and the ^{19}F contained drug and imaging agent used in MR imaging and spectroscopy. MR imaging pulse sequence, hardware and novel imaging agents have been developed to achieve more rapid and accurate quantitative methodologies for determination of imaging agents.

In the first part of the dissertation, a rapid T_1 and T_2 mapping technique ms-DSEPI-T12 is introduced to assess *in vivo* dynamic T_1 profile. Temporal resolution 15 sec has been achieved for the *in vivo* mice

experiments with voxel size of 1.0×1.0×2.0 mm^3. Comparing the conventional T_1 mapping methods, e.g., inversion recovery, which takes several to tens of minutes, ms-DSEPI-T12 can provide much higher temporal resolution.

In the second part, ^{19}F MR spectroscopy has been collected to monitor an ocular corticosteroid, TAP, with total dosage of 9 μmol using a rabbit model. Intravitreal and subconjunctival injections were used to deliver TAP into the rabbit eyes. The elimination half-lives of TAP *in vivo* and in postmortem rabbit eyes are 7.8±1.1, 17.2±2.1 Hr using intravitreal injection, and 0.5±0.1, 6.0±1.5 Hr using subconjunctival injection, which are used to investigate the possible ocular elimination pathway of TAP.

In the last part, ^{19}F MR imaging using a newly developed ^{19}F MR imaging agent, ^{19}FIT, was done on a 3T clinical system. For the mice experiment, conducted with voxel size 1.5×1.5×3.0 mm^3 and 5 min 9 sec imaging time, relatively high SNR (ranges from 10 to 60 in heart, liver and bladder) of the ^{19}F imaging is achieved.

TABLE OF CONTENTS

ABSTRACT iii

ACKNOWLEDGEMENTS vii

Chapter

1. MAGNETIC RESONANCE IMAGING IN MOLECULAR IMAGING AND DRUG DELIVERY RESEARCH 1

1.1 Introduction 1
1.2 ^{1}H MRI Using Paramagnetic Contrast Agents 2
1.3 ^{19}F MRI Using Fluorine Compounds 4

2. BASIC THEORY OF MAGNETIC RESONANCE IMAGING ... 6

2.1 Single Spin in External Magnetic Field - Classical Description 6
2.2 Single Spin in External Magnetic Field - Quantum Description 8
2.3 Bulk Magnetization 10
2.4 Signal Excitation 14
2.5 Spin – Lattice Relaxation Time 20
2.6 Spin – Spin Relaxation Time 24
2.7 The Bloch Equation 26
2.8 Signal Detection 28
2.9 Imaging Techniques 30
2.10 References 38

3. RAPID SIMULTANEOUS ACQUISITION OF T_1 AND T_2 MAPPING IMAGES USING MULTISHOT DOUBLE SPIN-ECHO EPI AND AUTOMATED VARIATIONS OF TR AND TE (MS-DSEPI-T12) 39

3.1 Introduction 39
3.2 Materials and Methods 41

3.3 Results and Discussion 51
3.4 Conclusions 66
3.5 Acknowledgements 66
3.6 References 67

4. OCULAR PHARMACOKINETICS STUDY OF A CORTICOSTEROID BY ^{19}F MR 70

4.1 Introduction 70
4.2 Materials and Methods 72
4.3 Results 77
4.4 Discussion 83
4.5 Conclusion 90
4.6 Acknowledgements 90
4.7 References 91

5. ^{19}F-MRI-BASED PHARMACOKINETICS ON A 3T CLINICAL MRI SYSTEM 94

5.1 Introduction 94
5.2 Materials and Methods 97
5.3 Results 100
5.4 Discussion 108
5.5 Conclusions 111
5.6 Acknowledgements 111
5.7 References 111

6. CONCLUSION 115

6.1 Summary 115
6.2 Limitations and Perspectives 117

ACKNOWLEDGEMENTS

First and foremost, I would like to express my deep and sincere gratitude to Professor Eun-Kee Jeong for being an outstanding advisor and mentor. I would also like to extend my thanks to rest of my committee, Professor Brian Saam, Professor Dennis Parker, Professor Eugene Mishchenko and Professor Gernot Laicher.

The members of UCAIR have contributed immensely to my personal and professional time at University of Utah. I am grateful to Dr. Seong-Eun Kim, Dr. Glen Morrell, Dr. Roy Rowley, Dr. June S. Taylor, Dr. Xianfeng Shi, Dr. Rock Hadley, Emilee Minalga and Joshua Kaggie for their invaluable comments and suggestions on this work.

I would like to acknowledge Dr. Zheng-Rong Lu, Dr. Yi Feng, Dr. Kevin Li, Dr. Sarah A. Molokhia, Dr. Bruce Yu and Dr. Zhongxing Jiang for their collaboration and help over the years.

Finally, I cannot forget to express appreciation to my family and friends for their tremendous support and understanding during my PhD studies.

CHAPTER 1

MAGNETIC RESONANCE IMAGING IN MOLECULAR IMAGING AND DRUG DELIVERY RESEARCH

1.1 Introduction

For conventional noninvasive medical imaging methods, such as magnetic resonance imaging (MRI) and computed tomography (CT), the imaging contrast is mainly from physical properties or the physiology of tissues. For example, the contrasts in most MR images are based on spin density, T_1 (spin-lattice relaxation time), T_2 (spin-spin relaxation time), and diffusivity of the hydrogen nuclei in the water molecules; CT images are based on the absorption or scattering of incident X-ray in tissue. The contrast sources determine that those imaging methods are mainly focused on detection of diseases on a macroscopic level, such as anatomical changes of the tissues.

With the rapid advances in molecular and cellular biology, understanding of the disease mechanism at the molecular or genetic level has been established. The molecular or genetic changes, which precede manifestation of disease, are the theoretical basis of early detection and diagnosis of the disease. The revealing of molecular pathways of the

underlying disease can lead to new treatment and therapy on the molecular level. Therefore, visualization and quantification of molecular biologic processes may be beneficial to molecular biology research, early clinical diagnosis, new therapy development and novel drug delivery investigation and evaluation. The demand has created a boom in molecular imaging.

MRI, as one of the major imaging modalities, has been increasingly used in molecular imaging approaches, because of its high spatial resolution and combination of anatomical and functional imaging. The basic theory of MRI is introduced in Chapter 2.

Using MRI to characterize specific biologic processes, a variety of imaging agents have been involved. Upon the introduction of the drug carrier molecules, such as the gadolinium-based contrast agent (GBCA) and the ^{19}F imaging agent, quantification of the concentration is the first step for further evaluation of the pharmacokinetics. Here, a brief review is introduced of paramagnetic T_1 contrast agent for ^{1}H imaging and fluorine compounds for ^{19}F imaging.

1.2 ^{1}H MRI Using Paramagnetic T_1 Contrast Agents

The mechanism of tracing paramagnetic T_1 contrast agents is based on the fact that the paramagnetic ion can shorten the proton T_1 relaxation time of the large pool of mobile water molecules existing in the human body. The relationships between the concentration of contrast agent, T_1 relaxation time and ^{1}H signal are described by equations 1.1 and 1.2. Here, C is the

concentration of contrast agent, R_1 a constant called T_1 relaxavity, T_{10} the T_1 value in the absence of contrast agent, S the ^1H signal intensity, S_0 the signal intensity from the fully recovered magnetization in thermal equilibrium, and TR the recovery time. Equation 1.2 only shows the simplest relationship between the ^1H signal and T_1; this relationship can be different for different imaging sequences.

$$R_1 C = \left(\frac{1}{T_1(C)} - \frac{1}{T_{10}}\right) \quad \ldots . (1.1)$$

$$S = S_0 \left[1 - \exp\left(-\frac{TR}{T_1}\right)\right] e^{-\frac{TE}{T_2}} \quad \ldots . (1.2)$$

Therefore, to trace and quantify paramagnetic contrast agents, it is necessary to measure precontrast and postcontrast images and T_1. However, it takes at least a few to tens of minutes to measure the T_1 using conventional imaging methods. Due to the lack of rapid T_1 measurement techniques, in practical pharmacokinetic studies, T_1 and T_2 are measured only on solution phantoms and used to estimate the concentration of GBCA. By doing so, several factors greatly affect the accuracy of the quantification, such as the nonlinear relationship between the ^1H signal and the contrast agent concentration, the intrinsic contrast sources in tissues and the dependence of imaging sequence and parameters.

In Chapter 3, a rapid T_1 measurement technique is introduced to address the problem.

1.3 ^{19}F MRI Using Fluorine Compounds

Besides paramagnetic T_1 contrast agents, fluorinated compounds are another family of MR imaging agents, which have been attempted for ^{19}F MRI in the past decade.

Heteronuclear MR imaging or spectroscopy has an advantage over the indirect monitoring of paramagnetic-ion based ^{1}H MRI because heteronuclear imaging allows direct detection and quantification of the imaging agent. NMR properties of several nuclei commonly used in MRI are listed in Table 1.1. Among the nuclei used in heteronuclear imaging, ^{19}F has several advantages over others, which include (1) the second highest gyromagnetic ratio after ^{1}H, which leads to relatively high sensitivity, (2) no detectable background ^{19}F MR signal from biological tissues, and (3) 100% natural abundance.

In Chapter 4, an application of ^{19}F MR spectroscopy is demonstrated to investigate the ocular pharmacokinetics of corticosteroids that contain a fluorine atom. Despite the strength, the low signal intensity is the biggest obstacle for application of ^{19}F MR. Therefore, the research on the MR side was focused on MR hardware improvement for ^{19}F MRI.

Chapter 5 presents a ^{19}F MRI pharmacokinetic study using a newly developed ^{19}F imaging agent, which overcomes several major problems in ^{19}F MRI using perfluorocarbon (PFC), such as low signal intensity, complex peak shapes, long T_1 and long *in vivo* retention time. Pharmacokinetic properties

and possible applications in drug delivery research of ^{19}F imaging agent have been investigated and discussed.

Table 1.1 NMR properties of nuclei commonly used in MRI.

Nuclei	Spin	Gyromagnetic Ratio (10^7 rad T^{-1} s^{-1})	Natural Abundance (%)	Relative Sensitivity*
^{1}H	1/2	26.752	99.985	1.00
^{13}C	1/2	6.728	1.108	1.76×10^{-4}
^{19}F	1/2	25.181	100.00	0.834
^{23}Na	3/2	7.080	100.00	9.27×10^{-2}
^{31}P	1/2	10.841	100.00	6.65×10^{-2}

*Relative sensitivity is calculated as the product of NMR sensitivity and the natural abundance.

CHAPTER 2

BASIC THEORY OF MAGNETIC RESONANCE IMAGING

Magnetic resonance imaging (MRI) utilizes the property of nuclear magnetic resonance to image nuclei of atoms inside the body. In this chapter, the basic theory of magnetic resonance imaging is introduced; more detail can be found in (1-4).

2.1 Single Spin in External Magnetic Field - Classical Description

If we consider a nucleus as a spinning ball with uniform charge distribution on the surface, due to the movement of the charge, the nucleus possesses a magnetic moment $\vec{\mu}$. In the presence of an external magnetic field $\vec{B}$, the nucleus will experience a torque $\vec{\mu}\times\vec{B}$. From classical mechanics, the torque equals the rate of the change of the angular momentum $\vec{J}$

$$\frac{d\vec{J}}{dt} = \vec{\mu} \times \vec{B} \quad \ldots.(2.1)$$

Since the angular momentum of the nucleus is related to the magnetic moment by $\vec{\mu} = \gamma \vec{J}$, where γ is the gyromagnetic ratio and its value varies between different nuclei, equation 2.1 can be rewritten as

$$\frac{d\vec{\mu}}{dt} = \vec{\mu} \times \gamma \vec{B} \quad \ldots.(2.2)$$

Assuming $\vec{B}$ is along the positive z direction, i.e. $\vec{B} = B_0 \hat{z}$, equation 2.2 can be written in components as

$$\begin{cases} \frac{d\mu_x}{dt} = \gamma B_0 \mu_y \\ \frac{d\mu_y}{dt} = -\gamma B_0 \mu_x \\ \frac{d\mu_z}{dt} = 0 \end{cases} \quad \ldots.(2.3)$$

The equations 2.3 can be written as

$$\begin{cases} \frac{d^2\mu_x}{dt^2} = -\omega_0 {\mu_x}^2 \\ \frac{d^2\mu_y}{dt^2} = -\omega_0 {\mu_y}^2 \\ \frac{d\mu_z}{dt} = 0 \end{cases} \quad \ldots.(2.4)$$

where $\omega_0 = \gamma B_0$.

Solving the differential equation 2.4, we get

$$\begin{cases} \mu_x(t) = \mu_x(0)\cos(\omega_0 t) + \mu_y(0)\sin(\omega_0 t) \\ \mu_y(t) = -\mu_x(0)\sin(\omega_0 t) + \mu_y(0)\cos(\omega_0 t) \\ \mu_z(t) = \mu_z(0) \end{cases} \quad \ldots.(2.5)$$

The results show that the x and y components of $\vec{\mu}$ rotate about the z-axis, which $\vec{B}$ lies on, with angular frequency $\omega_0 = \gamma B_0$, and the z component of $\vec{\mu}$ stays unchanged, which means the vector $\vec{\mu}$ rotates about vector $\vec{B}$ with angular velocity of $\vec{\omega} = -\gamma \vec{B}$, as shown in Fig. 2.1.

2.2 Single Spin in External Magnetic Field - Quantum Description

All nuclei have a spin quantum number of either half integer or integer. The spin quantum number $\vec{I}$ relates to the angular momentum $\vec{J}$ by the equation 2.6:

$$\vec{J} = \hbar \vec{I} \quad \ldots . (2.6)$$

The interaction energy of the nuclei with the external magnetic field $\vec{B} = B_0 \hat{z}$, which is called the Zeeman interaction, is given by

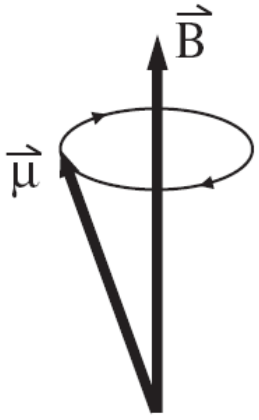

Figure 2.1 The motion of a single spin magnetic moment in an external magnetic field.

$$E = -\vec{\mu} \cdot \vec{B} = -\mu_z B_0 = -\gamma J_z B_0 = -\gamma \hbar I_z B_0 \quad \ldots . (2.7)$$

Therefore, a nucleus with a spin quantum number other than 0 will have $E = -\gamma \hbar B_0 m$, with m as the eigenvalue of I_z, $m = -I, -I+1, \cdots, I-1, I$. If we use $|m\rangle$ to represent different eigenstates of I_z, the time evolution of these eigenstates would be $\exp(-\frac{iE_m t}{\hbar})|m\rangle$. If the initial state is

$$\psi(0) = \sum_{m=-I}^{I} c_m |m\rangle \quad \ldots . (2.8)$$

at a later time t,

$$\psi(t) = \sum_{m=-I}^{I} c_m \exp(-\frac{iE_m t}{\hbar})|m\rangle \quad \ldots . (2.9)$$

then the expectation value of the components of $\vec{\mu}$ at an arbitrary time t would be

$$\begin{aligned} \langle \mu_n(t) \rangle &= \langle \psi(t) | \mu_n | \psi(t) \rangle \\ &= \sum_{m,m'} c_m^* c_m \gamma \hbar \langle m' | I_n | m \rangle \exp[\frac{it}{\hbar}(E_{m'} - E_m)] \quad \ldots . (2.10) \end{aligned}$$

where n represents x, y or z.

Take $I = \frac{1}{2}$ as an example, we have $m = \pm\frac{1}{2}$,

$$\langle \mu_x(t) \rangle = \gamma \hbar \left| c_{\frac{1}{2}} \right| \left| c_{-\frac{1}{2}} \right| \cos(\alpha - \beta + \gamma B_0 t)$$

$$\langle \mu_y(t) \rangle = -\gamma\hbar \left| c_{\frac{1}{2}} \right| \left| c_{-\frac{1}{2}} \right| \sin(\alpha - \beta + \gamma B_0 t)$$

$$\langle \mu_z(t) \rangle = \gamma\hbar \left(\left| c_{\frac{1}{2}} \right|^2 - \left| c_{-\frac{1}{2}} \right|^2 \right)/2 \quad \ldots . (2.11)$$

Here α and β are the arguments of the indexes $c_{\frac{1}{2}}$ and $c_{-\frac{1}{2}}$.

From the equations 2.11, we note that $\langle \mu_z(t) \rangle$ is independent of time, and $\langle \mu_x(t) \rangle$ and $\langle \mu_y(t) \rangle$ oscillate with frequency γB_0 while $\langle \mu_x(t) \rangle^2 + \langle \mu_y(t) \rangle^2$ remains constant. These show that $\langle \vec{\mu} \rangle$ is rotating about the z axis at a fixed angle from the z axis, which is exactly the rotation shown in the classical description.

2.3 Bulk Magnetization

In a bulk material containing a large amount of spins, a magnetization $\overrightarrow{M}$ is built as the vector sum of all the spin magnetic moments in the material as,

$$\overrightarrow{M} = \sum_{n=1}^{N} \vec{\mu}_n \quad \ldots . (2.12)$$

Here N indicates the total number of the spins.

In the absence of an external magnetic field, the orientation of the nuclear spins in the bulk material is random. Therefore $\overrightarrow{M}$ is zero; when the material is placed in a magnetic field $B_0\hat{z}$, using spin $\frac{1}{2}$ as an example, the nuclear spins will try to align with the external magnetic field, and the spin

will be oriented either parallel or antiparallel to the magnetic field as illustrated in Fig. 2.2.

Since m, the eigenvalue of I_z, can take the values from $-I$ to I, m is either $\frac{1}{2}$ or $-\frac{1}{2}$, so the interaction energy will split into $E_{\pm 1/2} = \mp\gamma\hbar B_0/2$ for two different m states and the energy difference between these two states is $\Delta E = \gamma\hbar B_0$. In thermal equilibrium at temperature T, the numbers of the spins in the two different states follow the Boltzmann Distribution, which gives

$$\frac{N_{1/2}}{N_{-1/2}} = \frac{\exp(-E_{1/2}/kT)}{\exp(-E_{-1/2}/kT)} = \exp(\Delta E/kT) \quad \ldots.(2.13)$$

where $N_{\pm 1/2}$ are the numbers of the spins in $m = \pm\frac{1}{2}$ states, k is the Boltzmann constant. Because for most cases in medical imaging, the temperature, T, is at body temperature of 310 K or room temperature of 298 K, ΔE is much smaller than kT, a high-temperature approximation can be applied to equation 2.13 as

$$\frac{N_{1/2}}{N_{-1/2}} = \exp(\Delta E/kT) \approx 1 + \frac{\Delta E}{kT} = 1 + \frac{\gamma\hbar B_0}{kT} \quad \ldots.(2.14)$$

Associated with

$$N_{1/2} + N_{-1/2} = N \quad \ldots.(2.15)$$

the population difference is described as,

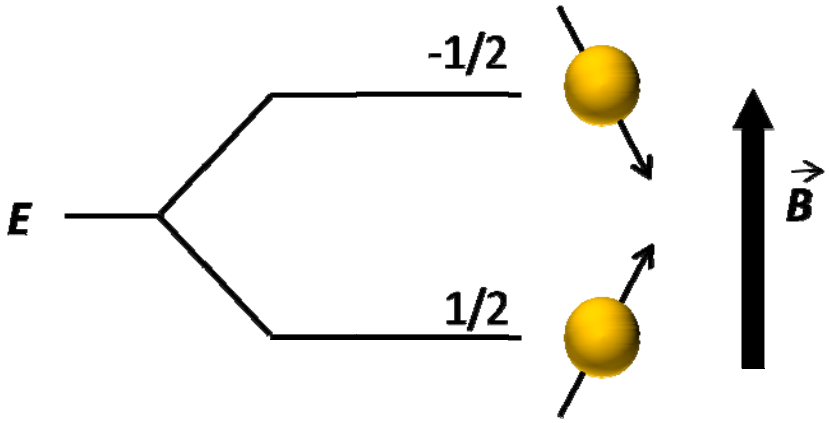

Figure 2.2 The energy splitting of a spin 1/2 system in the presence of an external magnetic field.

$$n = N_{1/2} - N_{-1/2} = N \cdot \frac{\gamma\hbar B_0}{2kT + \gamma\hbar B_0} \approx N \cdot \frac{\gamma\hbar B_0}{2kT} \quad \ldots.(2.16)$$

Therefore, in a sample of N spins, there are number $N \cdot \frac{\gamma\hbar B_0}{2kT}$ more spins oriented parallel than antiparallel to the external magnetic field.

Writing $\overrightarrow{M}$ in components, we have

$$\overrightarrow{M} = \sum_{n=1}^{N} \vec{\mu}_n = \sum_{n=1}^{N} \mu_{nx}\,\hat{x} + \sum_{n=1}^{N} \mu_{ny}\,\hat{y} + \sum_{n=1}^{N} \mu_{nz}\,\hat{z} \quad \ldots.(2.17)$$

According to quantum mechanics, the projections on the x-y plain of each spin magnetic moment $\vec{\mu}_n$ have random phase, which makes the two terms $\sum_{n=1}^{N} \mu_{nx}\,\hat{x}$ and $\sum_{n=1}^{N} \mu_{ny}\,\hat{y}$ vanish. Therefore, the magnetization can be written as,

$$\begin{aligned}
\overrightarrow{M} &= \sum_{n=1}^{N} \mu_{nz}\,\hat{z} \\
&= [N_{\frac{1}{2}} \cdot \frac{\gamma\hbar}{2} + N_{-\frac{1}{2}} \cdot \left(-\frac{\gamma\hbar}{2}\right)]\hat{z} \\
&= \left(N_{\frac{1}{2}} - N_{-\frac{1}{2}}\right) \cdot \frac{\gamma\hbar}{2}\,\hat{z} \\
&= N \cdot \frac{\gamma^2\hbar^2 B_0}{4kT}\,\hat{z} \quad \ldots.(2.18)
\end{aligned}$$

which complies with Curie's law $\overrightarrow{M} = C \cdot \overrightarrow{B}/T$ with the Curie constant $C = N\gamma^2\hbar^2/4k$.

Since each single spin magnetic moment follows equation 2.2, it would be logical that the vector sum $\vec{M}$ of all spin magnetic moments follow the similar equation

$$\frac{d\vec{M}}{dt} = \vec{M} \times \gamma \vec{B} \quad \ldots.(2.19)$$

2.4 Signal Excitation

2.4.1 Rotating Frame

The results in previous sections were derived in the laboratory frame. To simplify the description of excitation, we first introduced the concept of a rotating frame. If we move into a frame that rotates about $\vec{B}_0$ with angular velocity $\vec{\Omega}$, $\vec{\mu}$ can be expressed in the new frame as $\vec{\mu}(t) = \mu_x(t)\hat{x}' + \mu_y(t)\hat{y}' + \mu_z(t)\hat{z}'$,

$$\begin{cases} \frac{d\hat{x}'}{dt} = \vec{\Omega} \times \hat{x}' \\ \frac{d\hat{y}'}{dt} = \vec{\Omega} \times \hat{y}' \\ \frac{d\hat{z}'}{dt} = \vec{\Omega} \times \hat{z}' \end{cases} \quad \ldots.(2.20)$$

Therefore,

$$\frac{d\vec{\mu}(t)}{dt} = \frac{d\mu_x(t)}{dt}\hat{x}' + \mu_x(t)\frac{d\hat{x}'}{dt} + \frac{d\mu_y(t)}{dt}\hat{y}' + \mu_y(t)\frac{d\hat{y}'}{dt} + \frac{d\mu_z(t)}{dt}\hat{z}' + \mu_z(t)\frac{d\hat{x}'}{dt}$$

$$= \frac{d\mu_x(t)}{dt}\hat{x}' + \frac{d\mu_y(t)}{dt}\hat{y}' + \frac{d\mu_z(t)}{dt}\hat{z}' + \vec{\Omega} \times \left(\mu_x(t)\hat{x}' + \mu_y(t)\hat{y}' + \mu_z(t)\hat{z}'\right)$$

$$= \frac{\delta \vec{\mu}(t)}{\delta t} + \vec{\Omega} \times \vec{\mu}(t) \quad \ldots.(2.21)$$

where $\frac{\delta \vec{\mu}(t)}{\delta t}$ is the rate that $\vec{\mu}(t)$ changes in the new frame. Then equation 2.2 becomes,

$$\frac{\delta \vec{\mu}(t)}{\delta t} = \vec{\mu} \times \gamma \vec{B} + \vec{\mu} \times \vec{\Omega} = \vec{\mu} \times \gamma (\vec{B} + \frac{\vec{\Omega}}{\gamma}) \quad \ldots.(2.22)$$

In this rotating frame, the spin magnetic moment $\vec{\mu}$ experiences an effective field $\vec{B}_{eff} = \vec{B} + \vec{\Omega}/\gamma$, which $\vec{\mu}$ precesses about.

2.4.2 Classical Description

If an alternating magnetic field is turned on along the x-axis as $\vec{B}_1 = \hat{x} B_1 \cos \omega t$, it can be decomposed as the sum of two rotating magnetic fields, B_{cl} and B_{cc}, as shown in Fig. 2.3

$$\vec{B}_{cl} = \frac{1}{2} B_1 (\hat{x} \cos \omega t - \hat{y} \sin \omega t)$$

$$\vec{B}_{cc} = \frac{1}{2} B_1 (\hat{x} \cos \omega t + \hat{y} \sin \omega t) \quad \ldots.(2.23)$$

$\vec{\boldsymbol{B}}_{\boldsymbol{cl}}$ and $\vec{\boldsymbol{B}}_{\boldsymbol{cc}}$ are the components rotating clockwise and counterclockwise about the z-axis (as seen from the positive side of the z-axis) with angular frequency $\boldsymbol{\omega}$. Because $\vec{\boldsymbol{B}}_{\boldsymbol{cc}}$ rotates at an angular frequency different from the magnetization $\vec{\boldsymbol{M}}$ by $\boldsymbol{\omega} + \boldsymbol{\omega_0}$, $\vec{\boldsymbol{B}}_{\boldsymbol{cc}}$ is far from resonance with $\vec{\boldsymbol{M}}$ and can be neglected. Now $\vec{\boldsymbol{B}}_{\boldsymbol{cl}}$ is the only component we need to consider; we can treat it

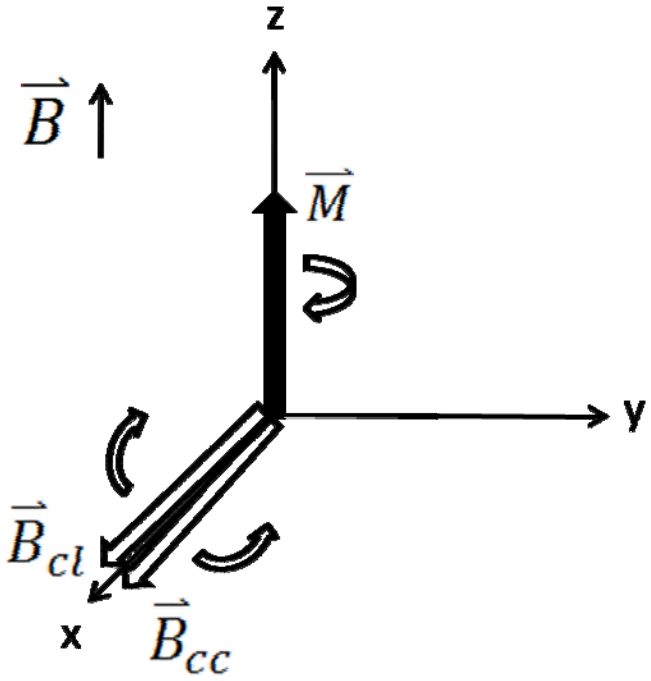

Figure 2.3 The decomposition of alternating B1 field, Bcl is the component that rotates clockwise, which is the same as the magnetization M, and Bcc is the component that rotates counter clockwise.

in a rotating frame that rotates with $\vec{\boldsymbol{B}}_{\boldsymbol{cl}}$. In this rotating frame, $\vec{\boldsymbol{B}}_{\boldsymbol{cl}}$ becomes stationary, and $\vec{\boldsymbol{M}}$ experiences the effective magnetic field $\vec{\boldsymbol{B}}_{\boldsymbol{eff}} = \left(\boldsymbol{B_0} - \frac{\boldsymbol{\omega}}{\boldsymbol{\gamma}}\right)\hat{\boldsymbol{z}}' + \boldsymbol{B_1}\hat{\boldsymbol{x}}'$, as shown in Fig. 2.4. In the simplest case with $\boldsymbol{\omega} = \boldsymbol{\gamma B_0}$, $\boldsymbol{B_0} - \frac{\boldsymbol{\omega}}{\boldsymbol{\gamma}}$ vanishes, $\vec{\boldsymbol{B}}_{\boldsymbol{eff}}$ is simply $\boldsymbol{B_1}\hat{\boldsymbol{x}}'$ and $\vec{\boldsymbol{M}}$ will rotate about $\boldsymbol{x}'$ axis at an angular frequency $\boldsymbol{\gamma B_1}$. After a given time t, the accumulated angle between $\vec{\boldsymbol{M}}$ and positive $\hat{\boldsymbol{z}}'$ axis, so called flip angle, will be $\boldsymbol{\gamma B_1 t}$. When the flip angle equals 90°, $\vec{\boldsymbol{M}}$ will lie on the $\hat{\boldsymbol{x}}'$ axis, and the magnetic field pulse is called a 90 degree pulse; when the flip angle equals 180°, $\vec{\boldsymbol{M}}$ will lie on negative $\hat{\boldsymbol{z}}'$ axis, and the magnetic field pulse is called a 180 degree pulse, and so on.

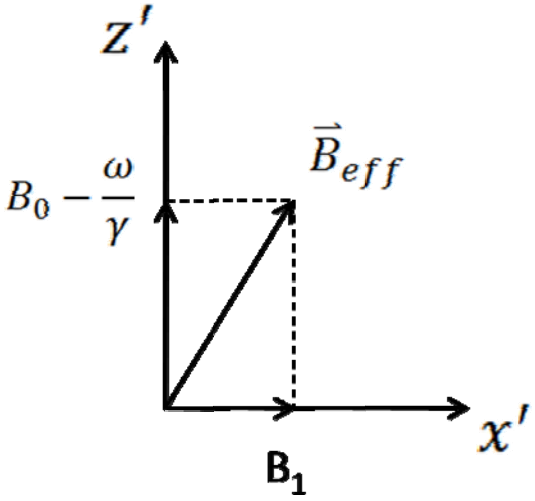

Figure 2.4 The effective magnetic field, B_{eff}, which the magnetization M experiences in the rotating frame that rotates with the same frequency as the alternating B_1 field.

2.4.3 Quantum Description

After B_1 field is turned on, the total magnetic field in the laboratory frame is

$$\vec{B} = B_1 \cos \omega t \, \hat{x} + B_1 \sin \omega t \, \hat{y} + B_0 \hat{z} \quad \ldots . (2.24)$$

The Hamiltonian of the interaction between $\vec{\mu}$ and $\vec{B}$ is

$$\begin{aligned} \mathcal{H} &= -\vec{\mu} \cdot \vec{B} \\ &= -(\mu_x B_1 \cos \omega t + \mu_y B_1 \sin \omega t + \mu_z B_0) \\ &= -\gamma \hbar [B_1 (I_x \cos \omega t + I_y \sin \omega t) + B_0 I_z] \quad \ldots . (2.25) \end{aligned}$$

Consider a function $A(\omega t) = \exp(-i\omega t I_z)\, I_x \exp(i\omega t I_z)$,

$$\frac{d^2A}{d(\omega t)^2} = \exp(-i\omega t I_z)\,(-iI_zI_y + iI_yI_z)\exp(i\omega t I_z)$$

$$= -\exp(-i\omega t I_z)\,I_x \exp(i\omega t I_z)$$

$$= -A \quad \ldots.(2.26)$$

By solving the differential equation $\frac{d^2A}{d(\omega t)^2} = -A$,

$$A(\omega t) = I_x \cos\omega t + I_y \sin\omega t \quad \ldots.(2.27)$$

combined with the definition of function $A(\omega t)$,

$$\exp(-i\omega t I_z)\,I_x \exp(i\omega t I_z) = I_x \cos\omega t + I_y \sin\omega t \quad \ldots.(2.28)$$

Substitute this into equation 2.25,

$$\mathcal{H} = -\gamma\hbar[B_1 \exp(-i\omega t I_z)\,I_x \exp(i\omega t I_z) + B_0 I_z] \quad \ldots.(2.29)$$

Therefore, the Schrodinger equation is

$$\frac{\partial\psi}{\partial t} = -\frac{i}{\hbar}\mathcal{H}\psi = i\gamma[B_1 \exp(-i\omega t I_z)\,I_x \exp(i\omega t I_z) + B_0 I_z]\psi \quad \ldots.(2.30)$$

Substitute ψ with $\psi' = \exp(i\omega t I_z)\,\psi$,

$$\frac{\partial\psi'}{\partial t} = i[\gamma B_1 I_x + (\omega + \gamma B_0 I_z)]\psi' \quad \ldots.(2.31)$$

by doing so, we are actually moving into a rotating frame ψ' can be obtained by rotating an angle ωt from ψ. For $\omega = \omega_0 = -\gamma B_0$,

$$\frac{\partial \psi'}{\partial t} = i\gamma B_1 I_x \psi' \quad \ldots . (2.32)$$

The solution is

$$\psi'(t) = \exp(i\gamma B_1 I_x t)\, \psi'(0) \quad \ldots . (2.33)$$

Since $\psi'(t) = \exp(i\omega t I_z)\, \psi(t)$ and $\psi'(0) = \psi(0)$,

$$\psi(t) = \exp(-i\omega t I_z) \exp(i\gamma B_1 I_x t)\, \psi(0) \quad \ldots . (2.34)$$

Therefore,

$$\langle \mu_z(t) \rangle = \int \psi^*(t) \mu_z \psi(t)\, d\tau$$

$$= \int \exp(i\omega t I_z) \exp(-i\gamma B_1 I_x t)\, \psi^*(0) \gamma \hbar I_z \exp(-i\omega t I_z) \exp(i\gamma B_1 I_x t)\, \psi(0)\, d\tau$$

$$= \gamma \hbar \int \psi^*(0) \exp(-i\gamma B_1 I_x t)\, I_z \exp(i\gamma B_1 I_x t)\, \psi(0)\, d\tau \quad \ldots . (2.35)$$

Similar to derivation of equation 2.28,

$$\exp(-i\gamma B_1 I_x t)\, I_z \exp(i\gamma B_1 I_x t) = I_z \cos \gamma B_1 t - I_y \sin \gamma B_1 t \quad \ldots . (2.36)$$

Thus

$$\langle \mu_z(t) \rangle = \gamma \hbar \int \psi^*(0) \left(I_z \cos \gamma B_1 t - I_y \sin \gamma B_1 t \right) \psi(0)\, d\tau$$

$$= \langle \mu_z(0) \rangle \cos \gamma B_1 t \quad \ldots . (2.37)$$

The result above shows $\langle \mu_z(t) \rangle$ oscillates in time, which satisfies the results derived classically - z magnetization rotates about $\hat{x}'$ axis in the rotating frame.

2.5 Spin – Lattice Relaxation Time

Spin – lattice relaxation time, T_1, is the characteristic time of the process that the spin system reestablishes the thermal equilibrium magnetization after RF excitation. The T_1 relaxation process is described by,

$$\frac{dM_z}{dt} = \frac{M_0 - M_z}{T_1} \quad \ldots . (2.38)$$

Once a spin is excited to a higher energy state from the ground state, it will always give up the energy and go back to the ground state eventually. Generally there are two mechanisms to realize the transition from excitation state to ground state – spontaneous and stimulated emissions. Because the spontaneous emission rate is proportional to the cube of the absorption energy, and the typical NMR absorption energy is in the order of μeV, the rate of spontaneous emission in NMR system is almost zero. Therefore, stimulated emission is the dominant mechanism for the transition of excited nuclear spins.

For a specific nucleus to achieve stimulated emission, an electromagnetic field oscillating at its Larmor frequency is required, which means the photon energy of the electromagnetic wave must be equal to the energy gap between its excitation state and ground state.

In general, for water hydrogen, the major source of the electromagnetic field is the magnetic field created by the neighboring hydrogen nuclear spin within the same water molecule, and the strength of the magnetic field is about 5 Gauss. Because of the thermal fluctuating random motion of the translation, rotation and vibration of the water molecule itself, and intermolecular collisions, the local magnetic field changes constantly in magnitude and direction, therefore becoming time varying. Taking the Fourier-transformation of this time varying magnetic field, one can get the spectral density $J(\omega)$, which can be considered as the density profile of molecules tumbling at different frequency. $J(\omega)$ is related to the correlation time τ_c of the randomly fluctuating motion of the molecule by equation 2.39,

$$J(\omega) = \frac{2\tau_c}{1 + (\omega\tau_c)^2} \quad \ldots.(2.39)$$

Fig. 2.5 gives $J(\omega)$ curves of three different τ_c. For free water where water molecules freely move around, the random motion of the water molecules is fast with a tumbling frequency of about 10^{11} Hz (5), which corresponds to the short τ_c curve. Since the proton Larmor frequency is 1.27×10^8 Hz at 3T, which is much lower than 10^{11} Hz, there is only a small portion of spectral density at the proton Larmor frequency. For water in soft tissues, due to the increased size of macromolecules, molecular tumbling is slowed down, i.e., τ_c becomes larger depending on the medium. In solid, water molecules are highly restricted, and τ_c is large. As shown in Fig. 2.5,

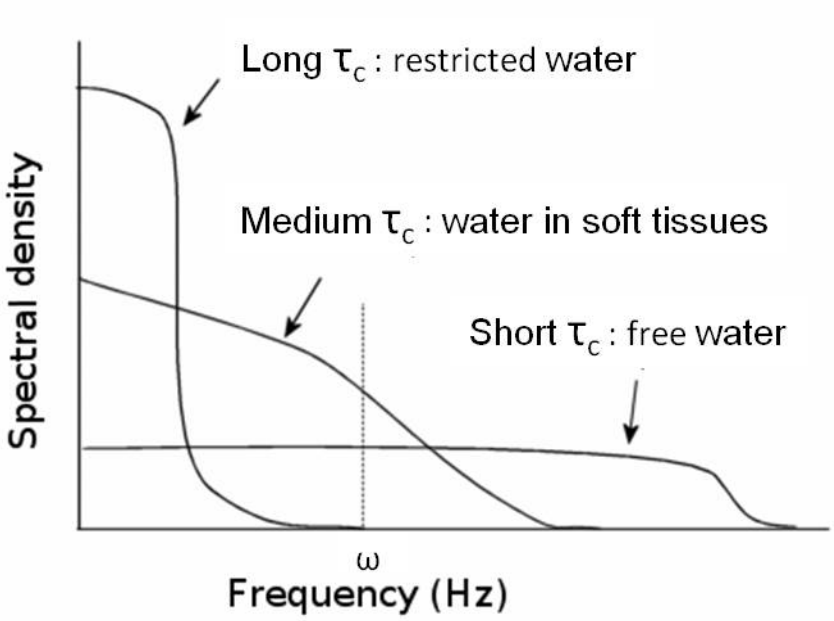

Figure 2.5 The spectral density of different correlation times, τ_c, which corresponds to water molecules in different environment.

compared with the intermediate τ_c, there is relatively less molecule tumbling at the proton Larmor frequency for both short τ_c and long τ_c, meaning less chance to take energy from the spin system and therefore longer T_1.

When paramagnetic T_1 contrast agents are introduced into the water, the unpaired electrons of paramagnetic ions play a key role in the T_1 relaxation process (6). For example, the electron configuration of gadolinium atom in Gd^{3+} based contrast agent is

$$1s^2\ 2s^2\ 2p^6\ 3s^2\ 3p^6\ 4s^2\ 3d^{10}\ 4p^6\ 5s^2\ 4d^{10}\ 5p^6\ 6s^2\ 4f^7\ 5d^1$$

as shown in Fig. 2.6. When it loses three outer shell electrons and becomes Gd^{3+} ion, there are still seven unpaired electrons in its 4f shell. Since the interaction between two spin magnetic dipoles is proportional to the

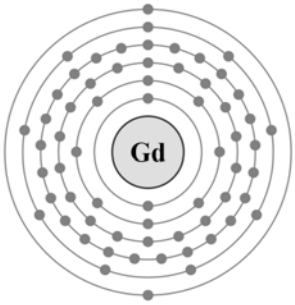

Figure 2.6 The electron shell diagram of gadolinium.

multiplication of the gyromagnetic ratios of both spins, the gyromagnetic ratio of the electron is roughly several hundred to one thousand times larger than the nuclear gyromagnetic ratio. Therefore, the interaction between electron spin and nuclear spin is much larger than it is between two nuclear spins.

Due to the extreme toxicity of free gadolinium ion, when we use Gd^{3+} as a contrast agent, it is necessary to chelate it with some organic ligands, such as DTPA (diethylenetriaminepentaacetic acid). Since the dipole-dipole interaction is inversely proportional to the cube of the distance between two dipoles, to have effect on T_1 relaxation of water proton, Gd^{3+} needs to be in close contact with water molecules, which is realized by the coordination binding between Gd^{3+} and water molecules. Gd^{3+} has nine coordination binding sites, in Gd-DTPA, eight of them are with DTPA, and there is only one left to interact with water molecules, as shown in Fig. 2.7. Since the binding is loose, water molecules can quickly attach to Gd^{3+}, complete the energy exchange, i.e., T_1 relaxation, then detach from Gd^{3+}. Therefore, even

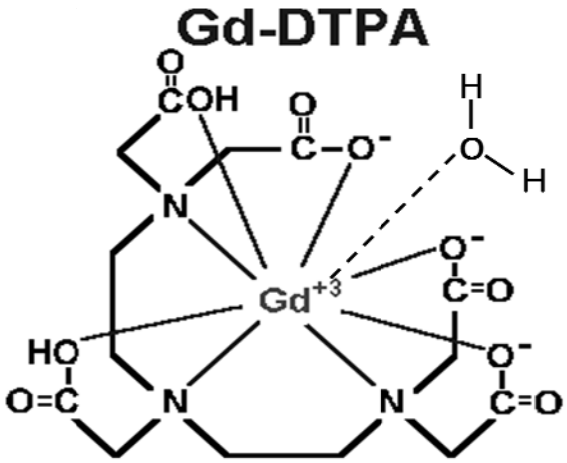

Figure 2.7 The chemical structure of Gd-DTPA. The dashed line represents the only coordination binding site left for water molecules.

though the concentration ratio between water molecules and Gd^{3+} is several thousand for a normal dosage, Gd^{3+} contrast agents can still exert strong influence to the T_1 relaxation process of water protons.

2.6 Spin – Spin Relaxation Time

Spin – spin relaxation time, i.e., T_2, is the characteristic time of the spin system to lose phase coherence and results in the decay of the magnetization in the transverse plane. The decay of the transverse magnetization relates to T_2 by equations,

$$\frac{dM_x}{dt} = -\frac{M_x}{T_2}$$

$$\frac{dM_y}{dt} = -\frac{M_y}{T_2} \quad \ldots.(2.40)$$

The rate of T_2 relaxation is increased due to spin diffusion and inhomogeneity of the local magnetic field surrounding individual spin.

Because of the dipole-dipole interaction between nuclear spins, the exchange of spin-states between two adjacent spins can occur. During this energy exchange, the spins will go through the energy conserving flip-flop transitions. In this way, the spin polarization transfer occurs from one location to another without actual physical translation of nuclei, which is known as spin diffusion.

In the bulk material, spins experience not only the magnetic field produced by an external magnet, but also the field from neighboring spins and the electron cloud around the nucleus. The sum of these magnetic fields is the local magnetic fields at each spin location. Random motion of these neighboring spins creates variations of the local magnetic field and therefore different local Larmor frequencies. When spins diffuse from one location to another, due to the different local Larmor frequency, the spins will accumulate different phases. On a macroscopic level, the magnetization, which is the vector sum of the spin magnetic moments, will eventually decay to zero while the phase of spins becomes completely random.

Because the time scale of molecule motion (on the order of picoseconds) is much smaller than T_2 ($\mu s \sim s$), within the time scale of T_2 relaxation, the spins will only see the average of the local magnetic field over this period. In general, the fluid molecules are less restricted than the molecules in solids. Therefore, the more active motion of the fluid molecules makes the time

average of the local field more uniform, which results in a longer T_2 in fluids than in solids.

2.7 The Bloch Equation

In section 2.3, we have explored the behavior of nuclear magnetization in an external magnetic field (equation 2.19). Taking into account the spin-lattice relaxation (equation 2.38) and spin-spin relaxation (equation 2.40), the Bloch's equation is modified,

$$\frac{d\,\vec{M}}{dt} = \vec{M} \times \gamma\,\vec{B} + \frac{(M_0 - M_z)\hat{z}}{T_1} - \frac{M_x\hat{x} + M_y\hat{y}}{T_2} \quad \ldots.(2.41)$$

which is the governing equation of motion for a magnetization. In a rotating frame, the equation (2.41) can be expressed as

$$\frac{d\,\vec{M}\,'}{dt} = \vec{M}\,' \times \gamma\,\vec{B}_{eff} + \frac{(M_0 - M_{z'})\hat{z}'}{T_1} - \frac{M_{x'}\hat{x}' + M_{y'}\hat{y}'}{T_2} \quad \ldots.(2.42)$$

Bloch's equation is very useful to describe the evolution of the magnetization under the influence of various magnetic fields, which include the static, spatially varying gradient, and RF magnetic fields.

During the RF pulse, consider the on-resonance case that the angular frequency of the rotating frame equals to the Larmor frequency of the nuclear spins. The effective magnetic field will be simply the B_1 field as,

$$\vec{B}_{eff} = B_1\hat{x}' \quad \ldots.(2.43)$$

Since the excitation duration is generally short compared to T_1 and T_2, we can ignore the terms related to T_1 and T_2, and equation 2.42 can be simplified and written in components as

$$\frac{dM_{x'}}{dt} = 0$$

$$\frac{dM_{y'}}{dt} = \gamma B_1 M_{z'}$$

$$\frac{dM_{z'}}{dt} = -\gamma B_1 M_{y'} \quad \ldots.(2.44)$$

Solving equation 2.44, we get

$$M_{x'} = 0$$

$$M_{y'} = M_0 \sin \gamma B_1 t$$

$$M_{z'} = M_0 \cos \gamma B_1 t \quad \ldots.(2.45)$$

This result is the same as the result we derived in section 2.4.

Immediately after the excitation, $\vec{B}_{eff}$ becomes zero in the same rotating frame, because of the absence of the excitation field. If we consider the transverse magnetization as a whole as $M_{x'y'}$, Bloch's equation becomes

$$\frac{dM_{z'}}{dt} = \frac{(M_0 - M_{z'})}{T_1}$$

$$\frac{dM_{x'y'}}{dt} = -\frac{M_{x'y'}}{T_2} \quad \ldots.(2.46)$$

Solving equation 2.46, we have

$$M_{x'y'} = M_{x'y'}(t = 0^+)\exp(-\frac{t}{T_2})$$

$$M_{z'} = M_0\left[1 - \exp\left(-\frac{t}{T_1}\right)\right] + M_{z'}(t = 0^+)\exp\left(-\frac{t}{T_1}\right) \quad \ldots.(2.47)$$

where $t = 0^+$ indicates the moment right after the excitation.

2.8 Signal Detection

According to Faraday's law, equation 2.48, changing magnetic flux will induce an electromotive force (EMF) in a closed circuit, and the EMF will generate a current inside the circuit.

$$\varepsilon = -\frac{d\phi}{dt} \quad \ldots.(2.48)$$

When the magnetization is excited, i.e., the magnetization is tipped from z direction onto the x-y plane, it will precess about the z-axis. For example, if we place a detection circuit in a plane perpendicular to the x-axis, as shown in Fig. 2.8, the x component of the precessing magnetization will oscillate in time, and then create an alternating magnetic flux through the area of the circuit, and therefore create an alternating current inside the circuit.

Fig. 2.9 shows the general steps for NMR signal detection. Once the alternating current is generated in the RF coil, the current signal will be sent to a low noise preamplifier, then the amplified signal will be mixed with an AC signal oscillating at the Larmor frequency in the demodulator, which is

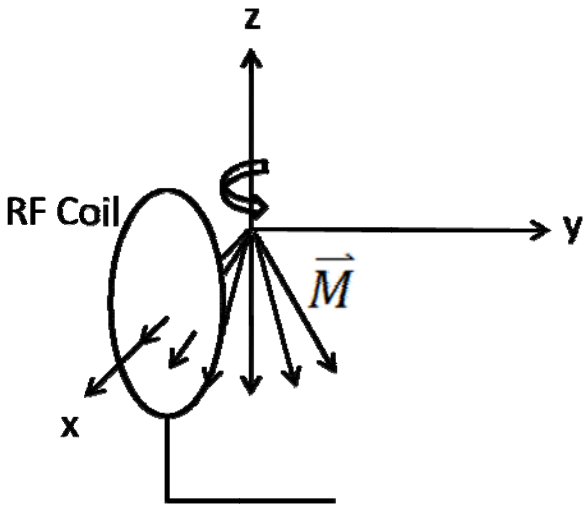

Figure 2.8 An RF coil is placed perpendicular to the x-axis. Due to the precession of the magnetization, the magnetic flux induced in the RF coil is alternating.

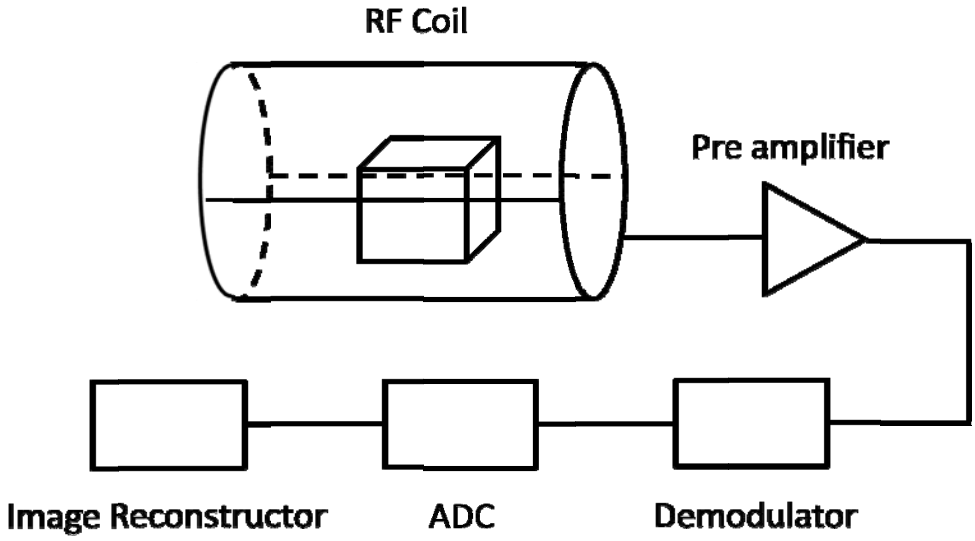

Figure 2.9 The basic hardware and steps for MR signal reception.

equivalent to moving into the rotating frame. At last, the signal is digitalized by an analog-to-digital converter (ADC) and sent to the computer for further processing, such as image reconstruction in MR imaging.

2.9 Imaging Techniques

2.9.1 Localization Techniques

To acquire images, we need an ability to distinguish signals that originate from different spatial locations. The hardware introduced for this purpose is called gradient coils. A gradient coil assembly includes three sets of coils, which can generate different magnetic field distributions along the z axis – the main magnetic field direction, and make the main magnetic field depend on locations along three independent directions, say the x, y and z directions, as illustrated in Fig. 2.10. These three gradient coils generate three orthogonal linear gradient fields G_x, $G_y$and G_z. Utilizing the gradient coils, there are three techniques to encode location information into the signals. They are slice selection, frequency encoding and phase encoding. A brief introduction of these techniques will be done as follows.

If we turn on a gradient in the $\hat{z}$ direction, which can be any direction in practice, by combining three gradient coil sets as $\hat{n} = G_x\hat{x} + G_y\hat{y} + G_z\hat{z}$, the main magnetic field B will have z dependence $B = B_0 + G_z z$ with a constant G_z, therefore, the Larmor frequency $\omega_0 = \gamma B_0$ will also depend on z. As shown in Fig. 2.11, when the excitation pulse only covers a certain bandwidth of frequency $\omega_1 \sim \omega_2$, then only spins residing between z_1 and z_2 are excited and

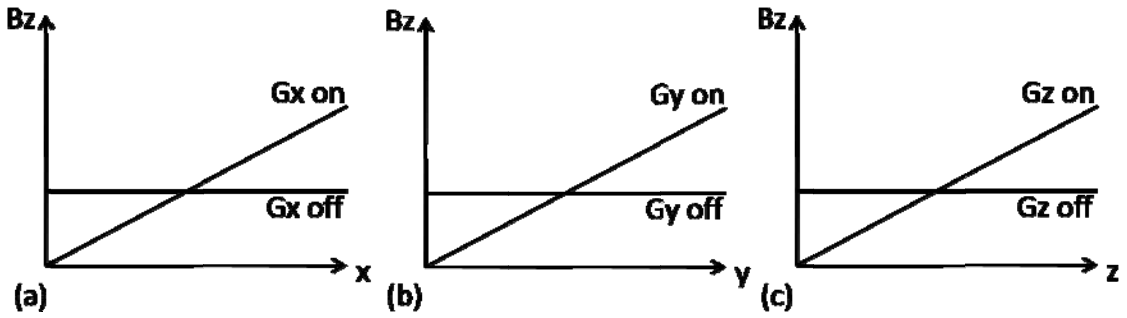

Figure 2.10 Gradient coils create Bz field gradients along x, y and z directions.

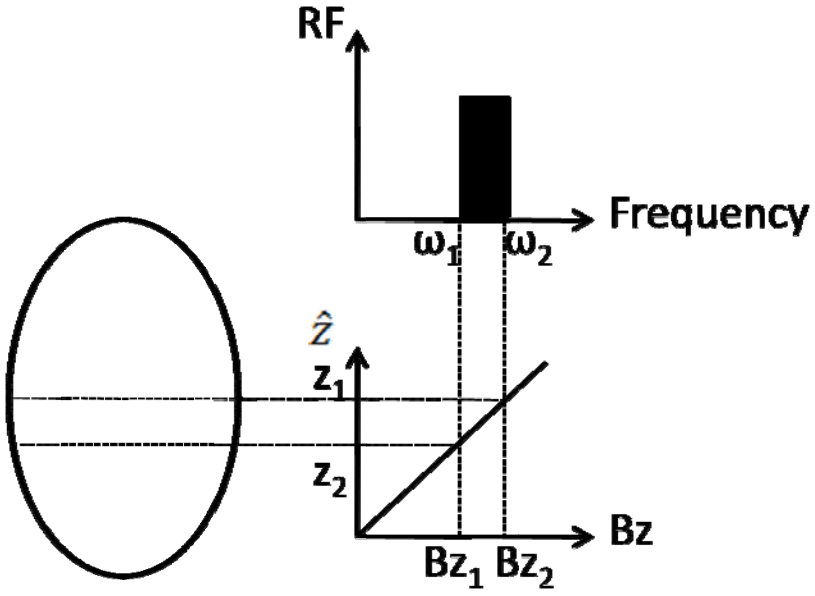

Figure 2.11 Illustration of mapping from RF excitation pulse frequency to the slice location.

contribute to the signal, while spins from all other locations give no signal. The technique is called slice selection.

If we assume that the main magnetic field is perfectly uniform within the region of the subject we are studying, then without any gradient fields, the spins from the entire subject will have the same Larmor frequency. The NMR signal, which is the sum of all individual magnetizations, is given by equation 2.49. Here, ρ is the spin density at the position x.

$$S(t) = \int \rho(x) \exp(-i\gamma B_0 t)\, dx = \int \rho(x) \exp(-i\omega_0 t)\, dx \quad \ldots . (2.49)$$

When the z-component of the magnetic field linearly varies along the x-axis by turning on G_x, the magnetic field becomes position dependent as, $\vec{B} = B_0 + G_x x$, so is the Larmor frequency of the spins as $\omega = \omega_0 + \gamma G_x x$. The signal can be expressed as,

$$S(t) = \int \rho(x) \exp(-i\omega_0 t) \exp(-i\gamma G_x x t) dx \quad \ldots . (2.50)$$

In the rotating frame, the term $\exp(-i\omega_0 t)$ is removed and the equation 2.50 becomes simplified as,

$$S(t) = \int \rho(x) \exp(-i\gamma G_x x t) dx \quad \ldots . (2.51)$$

Let $k_x = G_x t$, the equation 2.51 can be rewritten as

$$S(t) = \int \rho(x) \exp(-i\gamma k_x x) dx \quad \ldots . (2.52)$$

After Fourier transform,

$$\rho(x) = \int S(t) \exp(i\gamma k_x x) dk_x \quad \ldots.(2.53)$$

If we turn on the gradient, e.g., G_y along y direction, for a time T, because the spins at different locations will have different Larmor frequency, they will accumulate different phases $\gamma G_y y T$. Let $k_y = G_y T$, in the rotating frame,

$$S(t) = \int \rho(y) \exp(-i\gamma k_y y) dx \quad \ldots.(2.54)$$

After Fourier transform,

$$\rho(y) = \int S(t) \exp(i\gamma k_y y) dk_y \quad \ldots.(2.55)$$

Therefore, by using these methods, the signal contribution from different locations can be separated from each other and all together present an image in the spatial domain.

2.9.2 Imaging Pulse Sequences

Fig. 2.12 shows the schematic diagram of a spin echo pulse sequence. In the rotating frame, the magnetization initially lies along the z' axis. After a 90° RF pulse, the magnetization is flipped to the x'-y' plane, say along the y' axis, and starts to dephase due to the non-uniform local magnetic field. At time t=TE/2, the isochromats with different Larmor frequency have

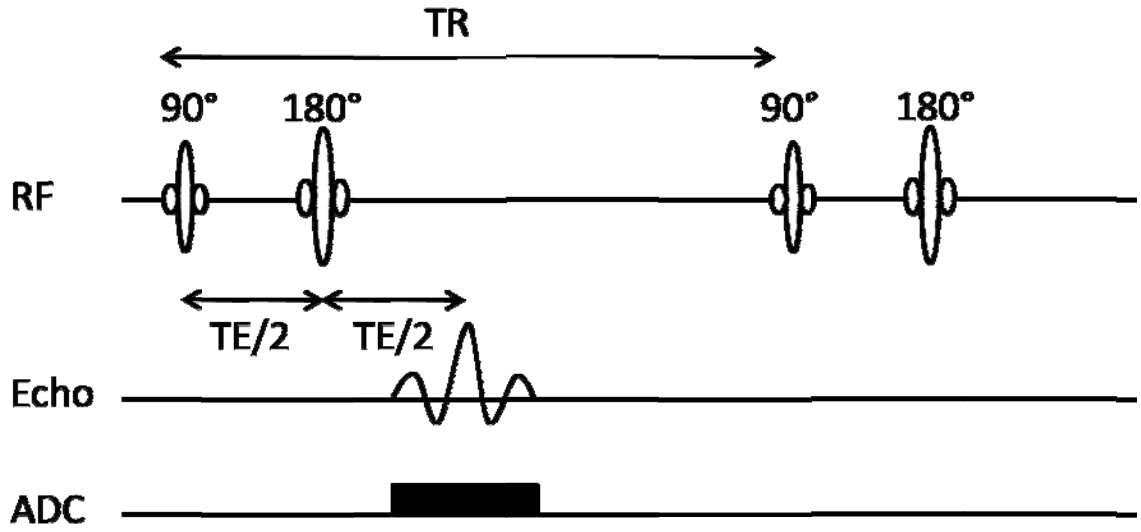

Figure 2.12 The pulse sequence diagram of a spin echo sequence.

accumulated different amounts of phase angle ϕ. During the moment, a 180° RF pulse is turned on, the phase angle ϕ becomes $-\phi$. Another time t=TE/2 later, all the isochromats will be refocused along the y' axis and a spin-echo is formed, as shown in Fig. 2.13. At the echo time t=TE, the signal will be collected to reconstruct the images.

Echo Planar Imaging (EPI) is a high speed imaging technique, in which multiple FID data with different k_y encodings are measured after a single excitation. A pulse sequence diagram of a spin echo type EPI sequence is presented in Fig. 2.14. The main difference between normal spin echo and a spin echo EPI sequence is the way k-space is filled. For normal spin echo, the signal collected at t=TE fills only one line of k-space, while for spin echo EPI, using a time varying gradient, the signal collected at t=TE can fill the entire k-space in a single shot. Only one echo is positioned at the spin-echo position and the rest are T_2*-weighted gradient echoes. The corresponding k-space trajectory of the EPI sequence in Fig. 2.14 is shown in Fig. 2.15.

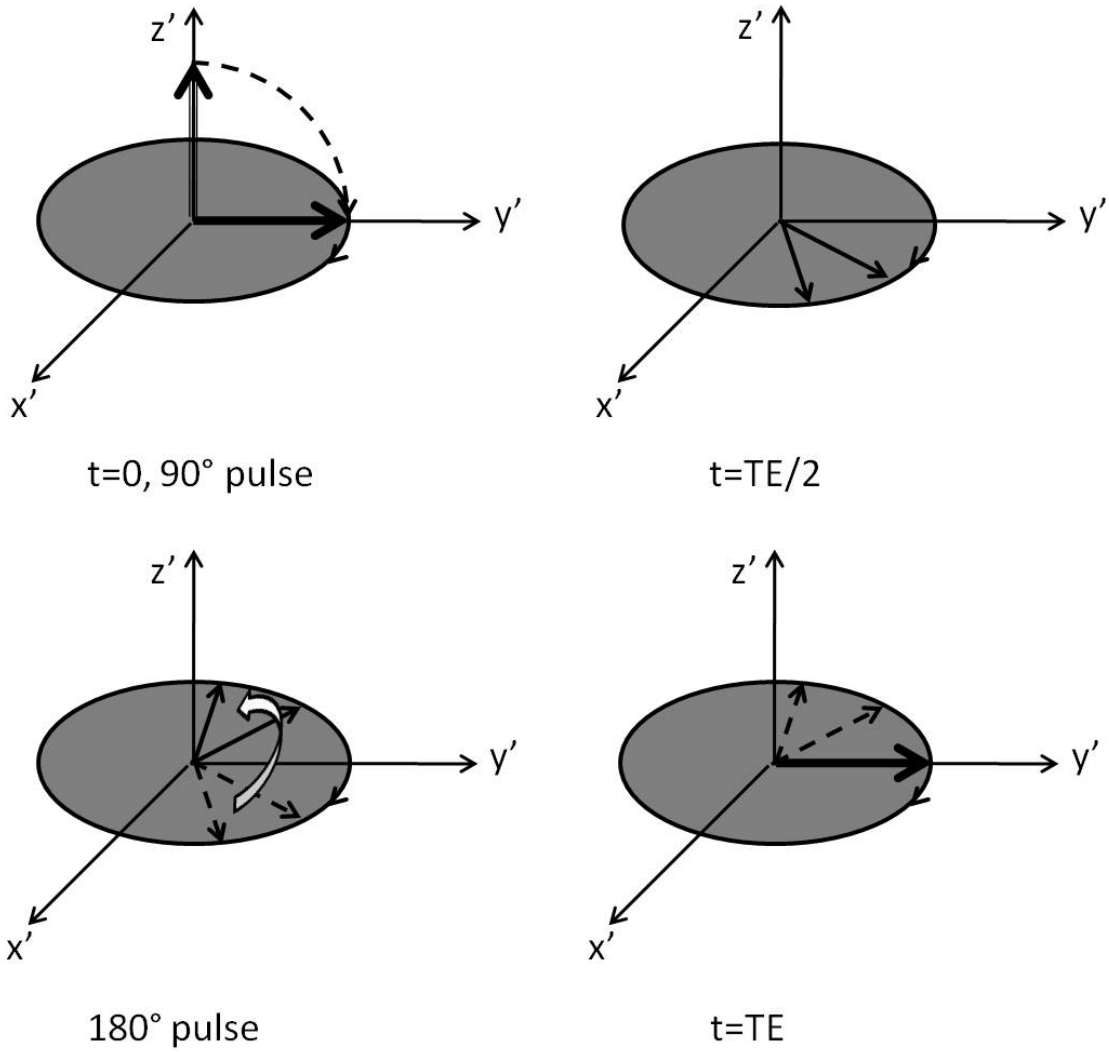

Figure 2.13 The diagram shows how the isochromats are being excited after the 90° pulse, dephasing and refocusing after the 180° pulse during the spin echo sequence.

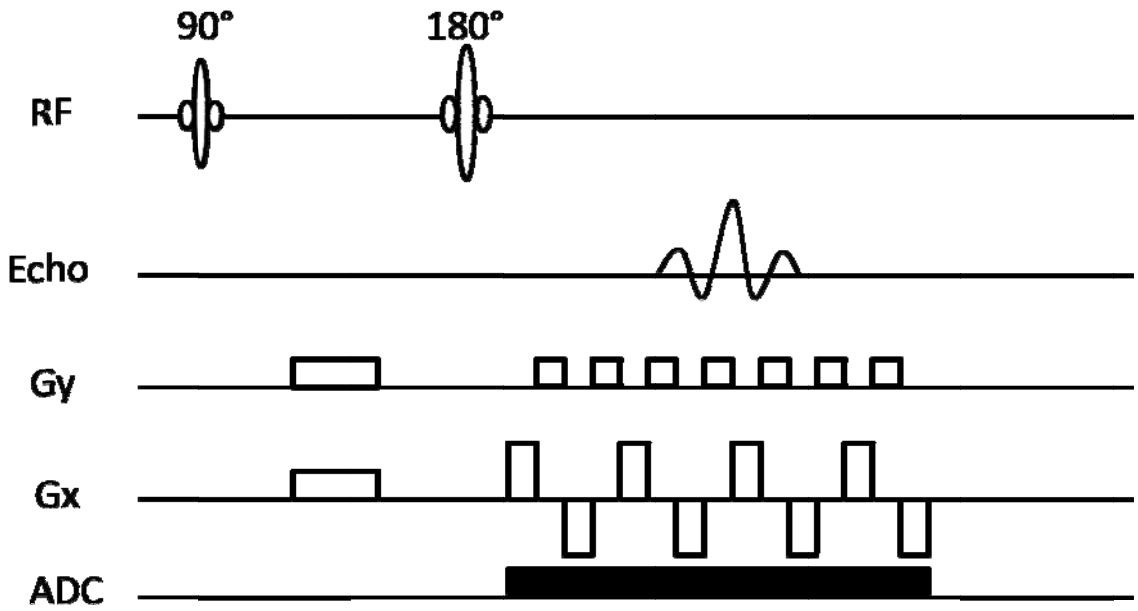

Figure 2.14 The pulse sequence diagram of a spin echo type EPI sequence.

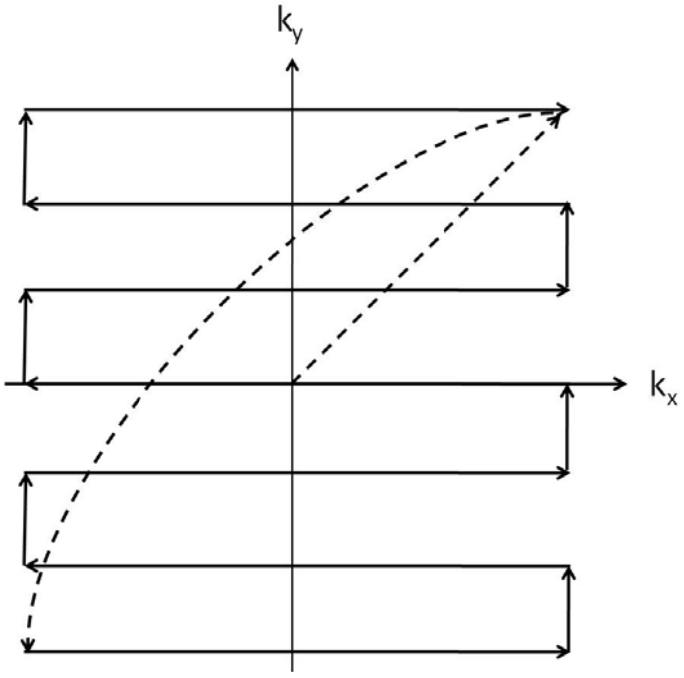

Figure 2.15 The k-space trajectory of the spin echo type EPI sequence illustrated in Fig. 2.14.

2.10 References

1. De Graaf RA. In vivo NMR spectroscopy : principles and techniques. Chichester, West Sussex, England ; Hoboken, NJ: John Wiley & Sons; 2007.

2. Haacke EM. Magnetic resonance imaging : physical principles and sequence design. New York: J. Wiley & Sons; 1999.

3. Liang Z-P, Lauterbur PC. Principles of magnetic resonance imaging : a signal processing perspective. New York: IEEE Press; 2000.

4. Slichter CP. Principles of Magnetic Resonance. New York: Springer-Verlag; 1990.

5. Bloembergen N PE, Pound R. Relaxation effects in nuclear magnetic resonance absorption. Physical Review 1948;73:23.

6. Koenig SH, Brown RD, 3rd. Relaxation of solvent protons by paramagnetic ions and its dependence on magnetic field and chemical environment: implications for NMR imaging. Magn Reson Med 1984;1(4):478-495.

CHAPTER 3

RAPID SIMULTANEOUS ACQUISITION OF T_1 AND T_2 MAPPING IMAGES USING MULTISHOT DOUBLE SPIN-ECHO EPI AND AUTOMATED VARIATIONS OF TR AND TE (MS-DSEPI-T12)

This chapter is based on the paper "Rapid simultaneous acquisition of T_1 and T_2 mapping images using multishot double spin-echo EPI and automated variations of TR and TE (ms-DSEPI-T12)," which was published in the journal NMR in Biomedicine in 2010, authored by Xin Liu, Yi Feng, Zheng-Rong Lu, Glen Morrell and Eun-Kee Jeong.

3.1 Introduction

Dynamic contrast enhanced MRI (DCE-MRI) has shown promise in detection and characterization of various tumors (1-8). DCE-MRI may provide information about important perfusion parameters such as vessel permeability (9), microvessel density (10), and washout which may allow more accurate characterization of benign versus malignant neoplasms. Change in relaxation rate ΔR_1 ($R_1 = 1/T_1$) is linearly related to Gd-DTPA concentration over a range of concentrations (11-13), and can be used to

estimate Gd-DTPA concentration. Pharmacokinetic information can be obtained from the time-variation of $\Delta R_1(\vec{r})$. Change in T_2 relaxation time is not usually measured in DCE MRI, because of the extended acquisition time which conventional T_2 measurement would require. However, the change of the concentration of the gadolinium based contrast agent causes the changes in both T_1 and T_2 relaxation times (14). The change in T_2 may be negligible at low concentration, but at higher concentration T_2 shortening may introduce error in the measurement of T_1. This effect may become significant in tumors, in which contrast achieves high concentrations due to high vessel density and blood supply induced by the tumor growth (15).

Spin echo or gradient recalled echo sequences with either inversion-recovery (IR) or saturation-recovery (SR) have been used for accurate T_1 and T_2 measurements. Their use has been limited to nondynamic imaging because of their long imaging times. Several alternative methods for T_1 mapping have been presented including 2D singleshot-EPI (2D ss-EPI) and variants (Look-Locker EPI, IR-EPI) which achieve better simultaneous spatial and temporal resolution (16-17). However, the spatial resolution using these rapid imaging methods is limited by susceptibility artifact (18-19). A multishot spin-echo EPI (ms-SEPI) sequence may be used to trade off imaging speed with severity of susceptibility artifact. Gradient-echo imaging with flip angle variation, may be used with reasonable temporal and spatial

resolutions (20). However, T_1 estimates obtained by this method are sensitive to RF inhomogeneity.

We present a rapid MR imaging method to simultaneously measure T_1 and T_2 using a multishot double spin-echo EPI sequence with automated variation of TR and TE (ms-DSEPI-T12) (21-22). Ms-DSEPI-T12 allows flexible adjustment of echo train length to compensate for differing severity of susceptibility artifact when imaging different areas of the body. Simultaneous measurement of T_1 and T_2 allows correction of T_2 effects on T_1 measurement. Our method is able to accurately measure T_1 with high spatial and temporal resolution, making it applicable to dynamic measurement of contrast concentration for pharmacokinetic studies.

3.2 Materials and Methods

3.2.1 Pulse Sequence Description

A multishot spin-echo EPI (ms-SEPI) sequence was used to implement the acquisition of the second echo and the automatic variations of the TR and TE on a Siemens 3T Trio clinical imaging system (Siemens Medical Solution, Erlangen, Germany). The schematic RF diagram of ms-DSEPI-T12 is shown in Fig. 3.1. The sequence begins with a presaturation pulse, followed by a saturation recovery delay interval τ. A 90-180° RF pulse pair is then played and a spin echo is acquired with echo-planar gradients scanning a portion of the k-space of a single slice, at minimum echo time. Then a second 180° is applied at a variable second echo time TE_i, and the same portion of k-space is

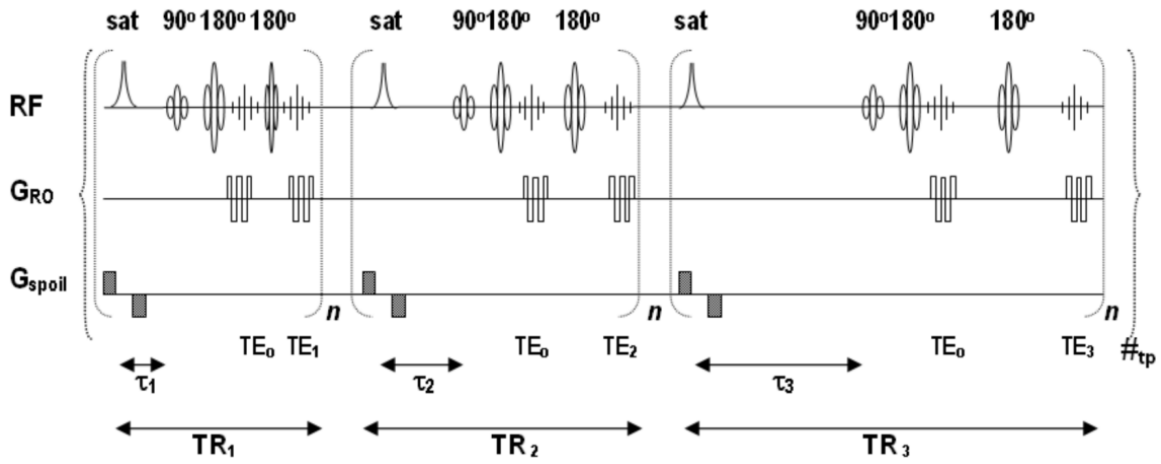

Figure 3.1. Pulse sequence diagram. τ_i is the saturation recovery time generating the i^{th} point on the T_1 recovery curve for estimation of T_1. TE_i is the echo time for the second echo, which is incremented as τ is incremented to give a set of second-echo images with varying T_2 weighting for T_2 estimation. Echotrain length after each 180° refocusing pulse is determined based on the desired acquisition speed and tolerated amount of image distortion, with longer echo train lengths giving shorter imaging time but more severe distortion secondary to susceptibility shifts. Each group of n TR's enclosed within a round bracket represents a complete k-space acquisition, giving an image for a particular recovery time τ_i (at minimum echo time $TE_{0)}$ and a second image for a particular second-echo echo time TE_n. The series of TR's within the curly bracket is repeated to give T_1 and T_2 maps at different successive time points.

reacquired. The sequence is repeated with no change in sequence timing to segmentally fill in the k-space for two complete images. This procedure is repeated with different saturation recovery times τ_i to create additional images. Each of the first-echo images supplies a time point along the T_1 recovery curve for estimation of T_1. The echo time TE_i of the second spin echo is incremented at the same time that the saturation recovery time is incremented. This creates a series of second echo images with differing T_2 weighting from which T_2 can be estimated. After a complete set of first- and second-echo images are obtained with varying recovery times τ_i and second echo times TE_i, the entire process is repeated to provide T_1 and T_2 estimates at successive time points, to allow analysis of enhancement kinetics.

The initial saturation pulse was performed with an adiabatic excitation followed by a gradient dephasing lobe. Better saturation may be obtained with a series of multiple saturation pulses and dephasing gradient lobes if needed.

Assuming that the longitudinal magnetization is completely destroyed by the saturation pulses at the beginning of the sequence, the signal equations for the first and second echoes for a given saturation recovery time τ_i and second echo time TE_i are:

first echo:

$$S_1(\vec{r}|\tau_i, TE_0) = S_0(\vec{r}) \cdot \left(1 - e^{-\frac{\tau_i}{T_1(\vec{r})}}\right) \cdot e^{-\frac{TE_0}{T_2(\vec{r})}} \quad \ldots.(3.1)$$

second echo:

$$S_2(\vec{r}|\tau_i, TE_i) = S_0(\vec{r}) \cdot \left(1 - e^{-\frac{\tau_i}{T_1(\vec{r})}}\right) \cdot e^{-\frac{TE_i}{T_2(\vec{r})}} \quad \ldots.(3.2)$$

A sequence of first echoes with various saturation times τ_i is used to calculate T_1, while a sequence of second echoes with various echo times TE_i is used to calculate T_2. Equations 3.1 and 3.2 can be written as:

$$S_1(\vec{r}|\tau_i, TE_0) = S'_0(\vec{r}) \cdot \left(1 - e^{-\frac{\tau_i}{T_1(\vec{r})}}\right), \qquad S'_0(\vec{r}) = S_0(\vec{r}) \cdot e^{-\frac{TE_0}{T_2(\vec{r})}} \quad \ldots.(3.3)$$

$$S_2(\vec{r}|\tau_i, TE_i) = S''_0(\vec{r}) \cdot e^{-\frac{TE_i}{T_2(\vec{r})}}, \qquad S''_0(\vec{r}) = S_0(\vec{r}) \cdot \left(1 - e^{-\frac{\tau_i}{T_1(\vec{r})}}\right) \quad \ldots.(3.4)$$

In the above equations, $S_0(\vec{r})$ represents the equilibrium longitudinal magnetization. The equilibrium signal $S_0(\vec{r})$ at a position $\vec{r}$ does not vary with T_1 and therefore does not change after administration of contrast, but depends on proton density, imaging voxel dimension, magnetic field strength, and temperature (23). $S'_0(\vec{r})$ is the signal intensity that would be obtained at the first echo time TE_0 after complete saturation recovery, i.e., for $\tau_i = \infty$. $S'_0(\vec{r})$ is also independent of T_1 and can be measured once during precontrast imaging with a long recovery time τ (~ $5T_1$) and then used as a data point in the calculation of T_1 for each subsequent time point in the sequence of dynamic images without being measured again. $S''_0(\vec{r})$ is the signal intensity that would be obtained for a given saturation recovery time τ_i with no T_2 decay, i.e., for TE = 0. Calculations of T_1 and T_2 are shown in Fig. 3.2.

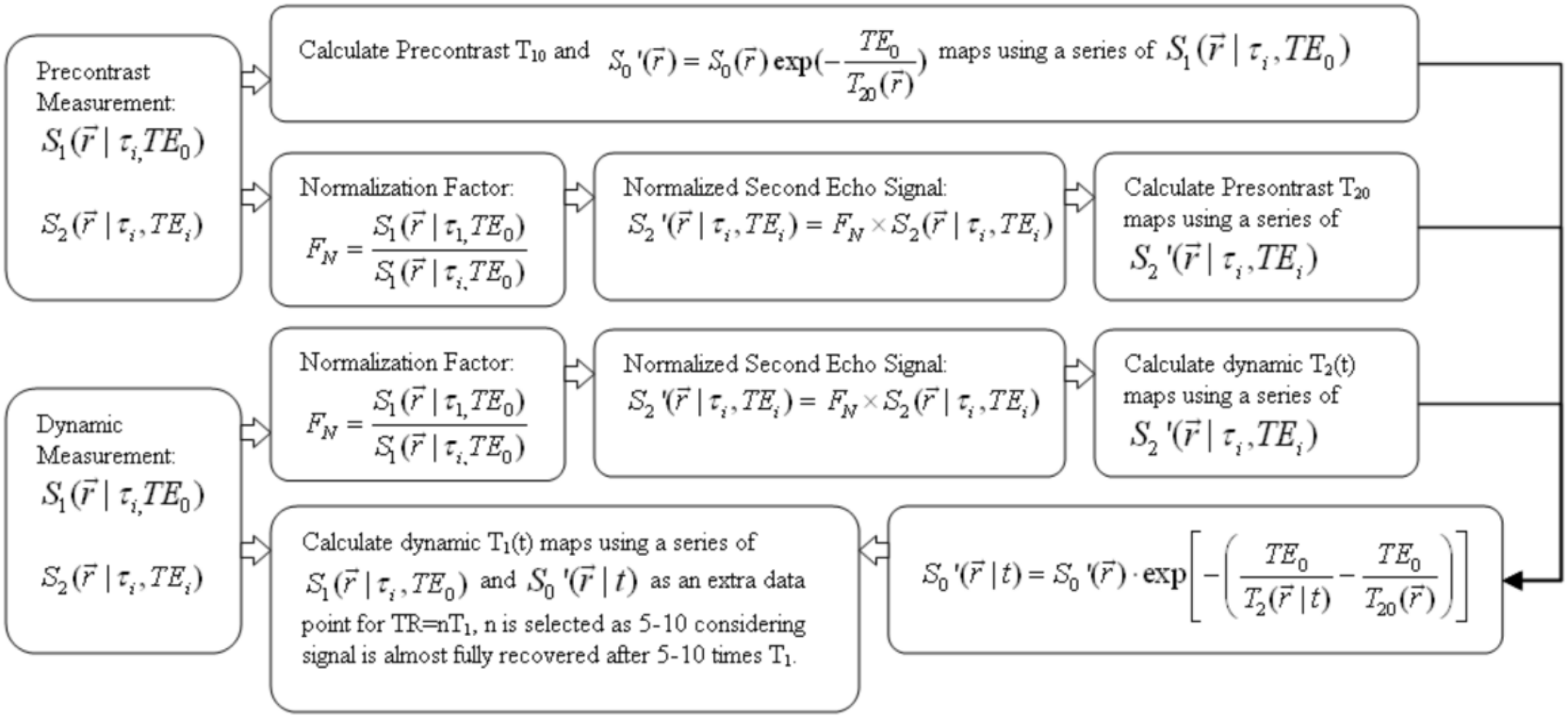

Figure 3.2. Precontrast and dynamic T_1 and T_2 calculation process flowchart.

3.2.2 Calculation of T_2 Using the Second Echoes

As shown in Fig. 3.2, both precontrast T_{20} and dynamic T_2 can be estimated from the sequence of second echoes $S_2(\tau_i, TE_i)$, each of which was obtained at a different echo time TE_i. A first echo $S_1(\tau_1, TE_0)$ can also be included in the points to be fitted for T_2 estimation. Because each second echo was obtained after a different saturation recover time τ_i, the second echo signal S_2 is dependent on T_1. To remove this dependence, the second echo signal intensity $S_2(\tau_i, TE_i)$ is normalized by the first echo time signal $S_1(\tau_i, TE_0)$ for the same τ_i. T_2 estimation was performed with least-squares fitting of the signal intensity samples to monoexponential decay.

3.2.3 Calculation of T_1 Using the First Echoes

The sequence of first echo images $S_1(\vec{r}|\tau_i, TE_0)$ traces the saturation recovery of longitudinal magnetization at various recovery times τ_i. For dynamic T_1 imaging, a limited number of saturation recovery times are measured, typically three or four, so that T_1 can be estimated in a short time to allow measurement of T_1 at multiple closely spaced time points. More saturation recovery times may be acquired during precontrast imaging. This allows accurate estimation of the fully recovered signal intensity $S'_0(\vec{r})$. This signal intensity does not change with T_1 shortening after administration of contrast, and can be used as an additional data point for estimation of T_1 at later time points without being measured at these time points. However, $S'_0(\vec{r})$ may change from its precontrast value on postcontrast scans because of

the T_2 shortening effect of contrast, causing a variable degree of T_2 decay during the fixed first echo time TE_o. Because T_2 is being simultaneously measured by our sequence, the effect of altered T_2 on $S'_0(\vec{r})$ can be easily removed.

3.2.4 Calculation of ΔR_1 Map Using T_1 Map

The dynamic change in $\Delta R_1(\vec{r}, t)$ at position $\vec{r}$ and time point t can be used to understand the kinetics of the delivery of the contrast agent based on paramagnetic ion. $\Delta R_1(\vec{r}, t)$ is calculated in pixel-by-pixel using the equation,

$$\Delta R_1(\vec{r}, t) = \frac{1}{T_1(\vec{r}, t)} - \frac{1}{T_1(\vec{r}, t = 0)} \quad \ldots.(3.5)$$

The calculation of T_1, T_2 and ΔR_1 for the acquired data was performed pixel-by-pixel, using custom mapping software developed in IDL (Interactive Data Language, Boulder, CO). The nonlinear Levenberg-Marquardt curve-fitting algorithm and an exponentially decaying fit were used to calculate T_1 and T_2, respectively. T_1, T_2, and $S'_0(\vec{r})$ of the precontrast data were calculated. For dynamic data, the spin-spin relaxation time T_2 was calculated after removing T_1 recovery effect from the second echo images. Then, this T_2 value was used to eliminate T_2 decay effect from $S'_0(\vec{r})$ that was obtained from the precontrast imaging data.

3.2.5 MR Imaging Experiments

All MR imaging experiments were performed on a clinical 3 T MRI system (Trio TIM System, Siemens Medical Solution, Erlangen, Germany). To validate the signal normalization process to remove T_1 recovery effect in T_2 measurement data, the ms-DSEPI-T12 mapping sequence was performed on a phantom filled with 0.1 mMol $MnCl_2$ solution, using a transmit/receive head coil. First, the sequence was run with the following schedule of saturation recovery times τ_i: 0.2, 0.25, 0.4, 0.8, 1.4, 2.2, 3.2 and 5.0 s. The first echo time TE_0 was 11.6ms, and the schedule of second echo times was: $TE_i = (15.1 + 10i)$ ms, $i = 1,2,\ldots 8$. This sequence was then repeated with a fixed saturation recovery time of 5.0 s, with the same schedule of TE_i's. An echotrain length (ETL) of 7 with 75 % asymmetric sampling was used for all phantom imaging, which resulted in the actual ETL of 5.

An MRI experiment was performed with three phantoms that were constructed of identical glass bottles with different $MnCl_2$ concentrations of 0.1, 0.3, and 0.6 mMol. Each bottle was filled with the same amount of solution to have equal coil loading. MR imaging was separately performed on each bottle positioned at the center of the head coil, using ms-DSEPI-T12 with imaging matrix 128×64, inplane spatial resolution 1.5×1.5 mm^2, and slice thickness 4.0 mm for 3 slices, saturation recovery times τ_i=0.09, 0.16, 0.25, 0.44, 0.73, 1.52, 2.31, 5.9 s and echo times TE_0=11 ms, $TE_i = (13 + 10i)$ ms, total imaging time 4 min 47 s. After imaging the first bottle, the second

and third bottles were placed in turn in the same location and separately imaged.

To evaluate the performance and accuracy of the new method, the same phantom was used to acquire T_1 measurement data with (1) ms-DSEPI-T12 for T_1 and T_2, (2) conventional inversion-recovery spin-echo (IR-SE) for T_1, and (3) conventional turbo-spin-echo (TSE) for T_2 measurements. For the ms-DSEPI-T12 sequence, imaging matrix was 128×64, inplane spatial resolution was 2.0×2.0 mm^2, and slice thickness was 3.0 mm for 5 slices, the schedule of saturation recovery times for the ms-DSEPI-T12 sequence was τ_i=0.22, 0.46, 0.7, 0.94, 1.33, 1.92, 2.91 and 4.9 s, with TE_0=10.0 ms and $TE_i = (12.7 + 10i)$, $i = 1 \sim 8$. For the inversion-recovery sequence and the TSE sequence, the same imaging matrix 128×64, inplane spatial resolution 2.0×2.0 mm^2, and slice thickness 3.0 mm for 5 slices was used. The inversion times TI used for the inversion-recovery sequence were 0.1, 0.4, 0.55, 0.6, 0.7, 0.8, 1.5 and 3.0 s with TR 10 s and TE 17 ms. TEs of 12, 23, 35, 47, 59, 70, 83, 94 and 105 ms were used for the TSE sequence with 5 s TR and ETL 9 to acquire T_2 maps. The imaging time for T_1 measurement was 5 min 36 s for ms-DSEPI-T12 measurement, while it was 16 min 39 s for IR-SE. The imaging time of T_2 measurement was 6 min 18 s for the TSE sequence.

The ms-DSEPI-T12 sequence was used to perform dynamic contrast enhanced T_1 measurement in mice. Female athymic nude mouse was cared for under the guidelines of a protocol approved by the University of Utah

Institutional Animal Care and Use Committee. The MDA-MB-231 human breast cancer cell line was purchased from the American Type Culture Collection (ATCC, Manassas, VA) and cultured in Leibovitz's L-15 medium with 2 mM L-glutamine and 10 % FBS at 37 °C in a humidified atmosphere of 5 % CO_2. The cells were allowed to grow to about 90 % confluence and then resuspended in DMEM medium. The cell number was adjusted to 106 cells/ml, and the cells were mixed with an equal volume of Matrigel (Becton-Dikinson, Franklin Lakes, NJ). The Matrigel mixtures, containing approximately 2×10^5 cells in 0.2 ml, were implanted subcutaneously in the flanks of the mouse. Each implantation generated a tumor. Tumor size reached 0.5–1.5 cm in diameter 21 days after cell implantation.

The ms-DSEPI-T12 sequence was applied to acquire dynamic images in the axial plane with echotrain length of 3, imaging matrix 64×28, inplane spatial resolution 1.0×1.0 mm^2, and slice thickness 2.0 mm, for 4 slices. A Siemens human wrist coil was used. Precontrast T_1 mapping data were acquired with 8 different saturation recovery times τ_i=0.25, 0.5, 0.75, 1.0, 1.4, 2.2, 3.2, and 5.0 s, first echo TE of 8ms, and second echo times of TE_i = (9 + 10*i*) ms, the imaging time was 2 min 56 s. For postcontrast dynamic imaging, TRs of 200, 500, and 750 ms and TE_0=8 ms, TE_i = (4 + 15*i*) ms were used. The imaging time for each time point was 15.0 s. Slice interleaving was limited by the shortest TR, i.e., 200 ms in the current protocol.

3.3 Results and Discussion

The plots in Fig. 3.3 show the signal intensities of the second echoes of the fixed (◊) and the variable (*) recovery times, and after normalization (□) by the signal intensities of the first echoes. The normalized signal intensity values (□) obtained with variable saturation recovery times τ_i match the second echo signal intensities obtained with the constant saturation recovery time of 5 s, demonstrating that the effect of varying saturation recovery time on T_2 estimation has been successfully removed.

The series of three phantom studies simulates the effect of imaging a single structure with time-varying T_1. Prescan calibration was performed only for the first bottle and transmitter and receiver gains were held constant for the remaining bottles.

T_2 was estimated for the three bottles as described above. The equilibrium signal $S'_0(\vec{r})$ for the first bottle was measured at long saturation recovery time (5.9 s). This value was then combined with the measured T_2 of each bottle to give a calculated value for the equilibrium value $S'_0(\vec{r})$ for each bottle, which was compared to the actual measured value. There was excellent agreement between the measured equilibrium values $S'_0(\vec{r})$ of the second and third bottles and the values calculated from $S'_0(\vec{r})$ of the first bottle and the T_2 of each bottle, as shown in Table 3.1. This result confirms that the equilibrium value $S'_0(\vec{r})$ can be measured once in the precontrast phase of a dynamic contrast enhanced imaging experiment and then used to

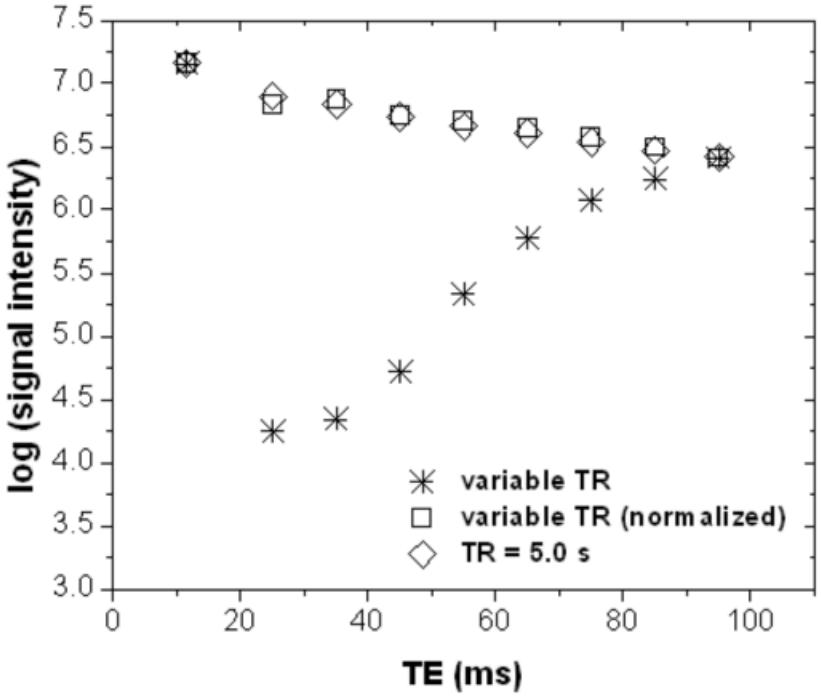

Figure 3.3. Phantom study validating correction of second echo intensity for varying saturation recovery time. Stars represent uncorrected second echoes, squares represent second echoes normalized by first echoes to remove effects of variable saturation recovery times, and diamonds represent second echoes obtained with constant saturation time of 5s. Normalization removes the effect of varying saturation recovery, allowing estimation of T_2 from second echoes with varying echo time.

Table 3.1. Measured vs. calculated equilibrium signal intensity $S'_0(\vec{r})$, representing the signal intensity measured at very large saturation recovery time ($\tau_i \rightarrow \infty$). Good agreement between calculated and measured values shows that this point can be measured once and then calculated for subsequent time points from the measured T_2 values.

Concentration (mMol)	T_2 (ms)	$S_o'(r)$ (calculated)	$S_o'(r)$ (measured)
0.1	57.1±5.5	-	2196.2±60.3
0.3	29.7±2.6	1838.6±50.5	1864.3±50.7
0.6	15.6±1.5	1315.5±36.1	1329.5±44.3

calculate $S'_0(\vec{r})$ for subsequent postcontrast time points, without actually being measured at these later time points. As demonstrated in Fig. 3.4, T_2 effects of increasing contrast concentration cause marked decrease in the equilibrium signal $S'_0(\vec{r})$ as well as T_1 shortening.

An MR imaging experiment was performed on a fluid phantom to compare the T_1 relaxation times calculated from a data set of 8 well spaced saturation recovery times and a set with three short and one long saturation recovery times, which would represent the precontrast and the dynamic data sets of a dynamic contrast enhanced study. Postcontrast measurement at a limited number of saturation recovery times allows better temporal resolution in the T_1 estimation for dynamic imaging. Shorter saturation recovery times allow shorter TR and therefore faster imaging. The longest saturation recovery time point can be calculated from the precontrast data and the T_2 of the current acquisition, substantially shortening the required imaging time. The measured signal intensities for varying saturation recovery times τ_i are shown in Fig. 3.5. The solid line represents the T_1 recovery curve fit to all eight data points. The dashed line represents the T_1 recovery curve fit to only the first three data points plus the last data point. The resultant T_1 values were 445.0±2.1 and 440.0±3.1 ms with the full (8 τ_i's) and the partial (3 measured τ_i's and 1 calculated from precontrast T_1/T_2 measurements) data sets, respectively. The fractional difference between the resultant T_1 values of two methods was less than 2 %. This experiment shows

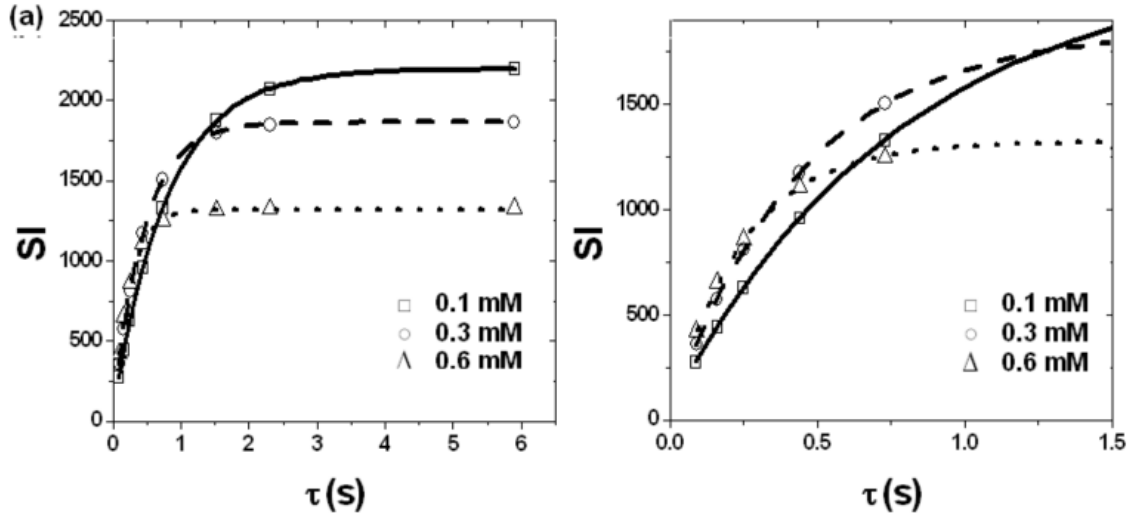

Figure 3.4. Plots of the measured signal intensities for three concentrations of $MnCl_2$ solutions. Increasing concentration gives faster T_1 recovery but lower equilibrium signal intensity $S'_0(\vec{r})$ because of T_2 shortening. As shown in Table 3.1, the last time point (5.9 s in the above plots) can be measured at one concentration and then calculated for the other concentrations, significantly shortening the required imaging time. Plot b) is an enlarged view of plot a).

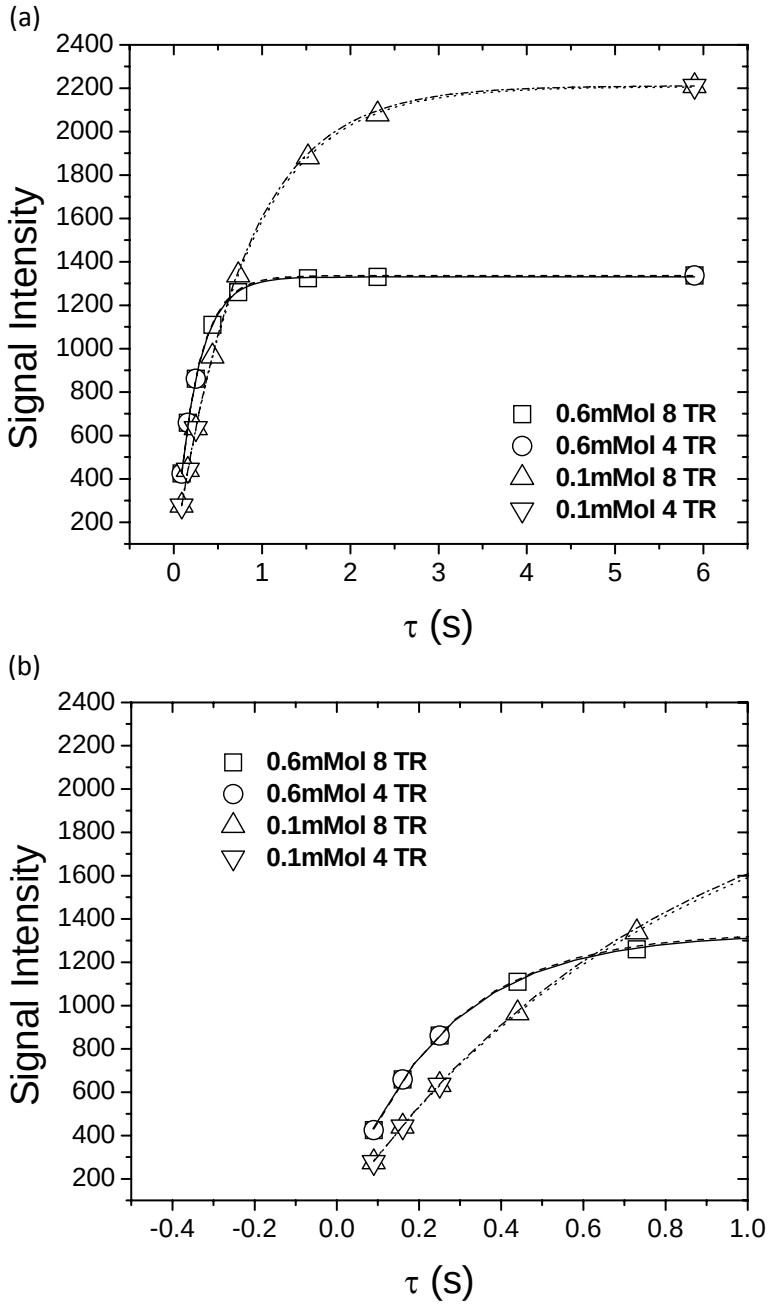

Figure 3.5. T_1 recovery plot of eight saturation recovery times, with T_1 recovery curve fitted to all eight points (dashed line) vs. only the first three points and the last point (dotted line). The solid line represents fitting to only the first three points without the last point, showing the necessity of the last point for accurate T_1 estimation. However, this last point does not need to be measured during postcontrast dynamic imaging but instead can be calculated from its precontrast value and the measured T_2. Plot b) is an enlarged view of plot a).

that the accurate value of T_1 can be measured using only a few short τ_i's and the semiempirical $S'_0(\vec{r})$ for rapid dynamic MR imaging.

The T_1 profiles along the dotted line on T_1 maps of a fluid phantom in Fig. 3.6a using ms-DSEPI-T12 and IR-SE are overlaid in Fig. 3.6b. The mean values of T_1 and T_2 in a region-of-interest at the center of the object were measured as 867.9±34.1 ms and 872.0±5.9 ms using ms-DSEPI-T12 and IR-SE, and 57.6±2.0 ms and 76.1±2.8 ms using ms-DSEPI-T12 and TSE, respectively. T_2 value measured using ms-DSEPI-T12 was 24.3% lower than that measured using TSE. Both methods used a similar range of echo time TEs, 10 ~ 94 ms for ms-DSEPI-T12 and 12 ~ 105 ms for TSE. T_1 relaxation time measured by the two methods was nearly equal, although the variance was somewhat increased in ms-DSEPI-T12 technique, particularly near the edge and outside of the RF coil. This was because the SNR in the source T_1 and T_2 weighted images were significantly reduced in ms-DSEPI-T12 images compared to IR-SE images due to the short imaging time.

The dotted rectangular box in Fig. 3.6a indicates the position of the coil. The homogeneity of the B_1 field was poor near the right end of the coil. Since the phantom is uniform across the dotted line, the uniform T_1 values across the dotted line measured using ms-DSEPI-T12 indicates that ms-DSEPI-T12 would not suffer much from the RF inhomogeneity, except for the increased variance due to the decreased SNR.

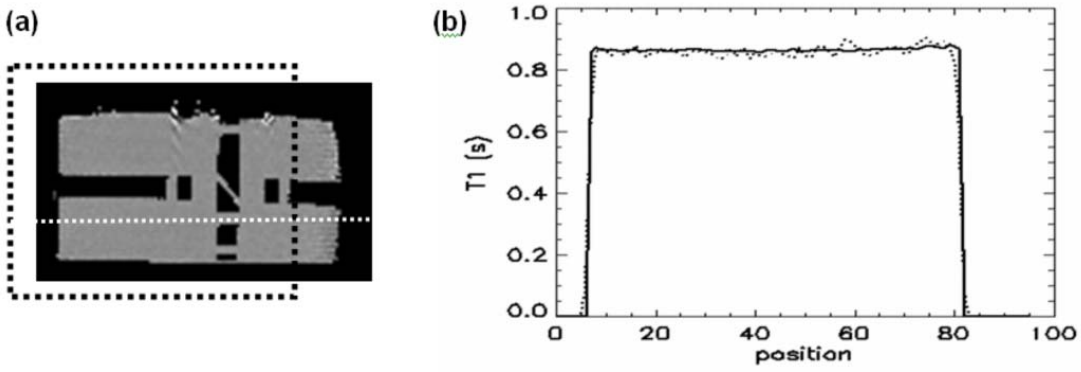

Figure 3.6. The profiles of T_1 values measured along a central line on T_1 maps of a phantom acquired with the ms-DSEPI-T12 mapping sequence (dotted line) and IR-SE (solid line). The dotted rectangular box on the T_1 map image (a) indicates the position of the head coil.

Phantom studies demonstrated excellent agreement between the measured T_1 values measured using ms-DSEPI-T12 and conventional inversion recovery technique. T_2 values measured using ms-DSEPI-T12 were lower than those measured using TSE sequence, which may be due to the translation diffusion under background and imaging gradient (23). A simulation was performed to evaluate the error in T_1 calculation propagated from the error in underestimated T_2 using ms-DSEPI-T12. According to equation 3.6,

$$S'_0(\vec{r}|t) = S'_0(\vec{r}) \cdot \exp[-(\frac{TE_0}{T_2(C)} - \frac{TE_0}{T_{20}})]$$

$$= S'_0(\vec{r}) \cdot \exp[-TE_0(\frac{1}{T_2(C)} - \frac{1}{T_{20}})]$$

$$= S'_0(\vec{r}) \cdot \exp[-TE_0 \cdot R_2 \cdot C] \quad \ldots.(3.6)$$

and the fact that T_1 was calculated by curve fitting a series of $S'_0(\vec{r}|t)$, the error in T_1 was simulated with respect to different fractional error in T_2 estimation (Fig. 3.7a) and local concentration of the Gd-based contrast agent C (Fig. 3.7b), and using TE_0 10 ms, T_{20} 50 ms, and a spin-spin relaxivity R_2 of 10 L/mmol/sec. The same fractional error was used for both T_{20} and $T_2(C)$. For Fig. 3.7a, concentration C = 1 mmol/L, for Fig. 3.7b we assume 25% underestimation in both T_{20} and $T_2(C)$.

Plots in Fig. 3.7 indicate that large fractional error in T_2 estimate leads to much smaller fractional error in T_1 calculation. Even for a high local contrast agent concentration C = 1 mmol/L, which can be hardly reached in

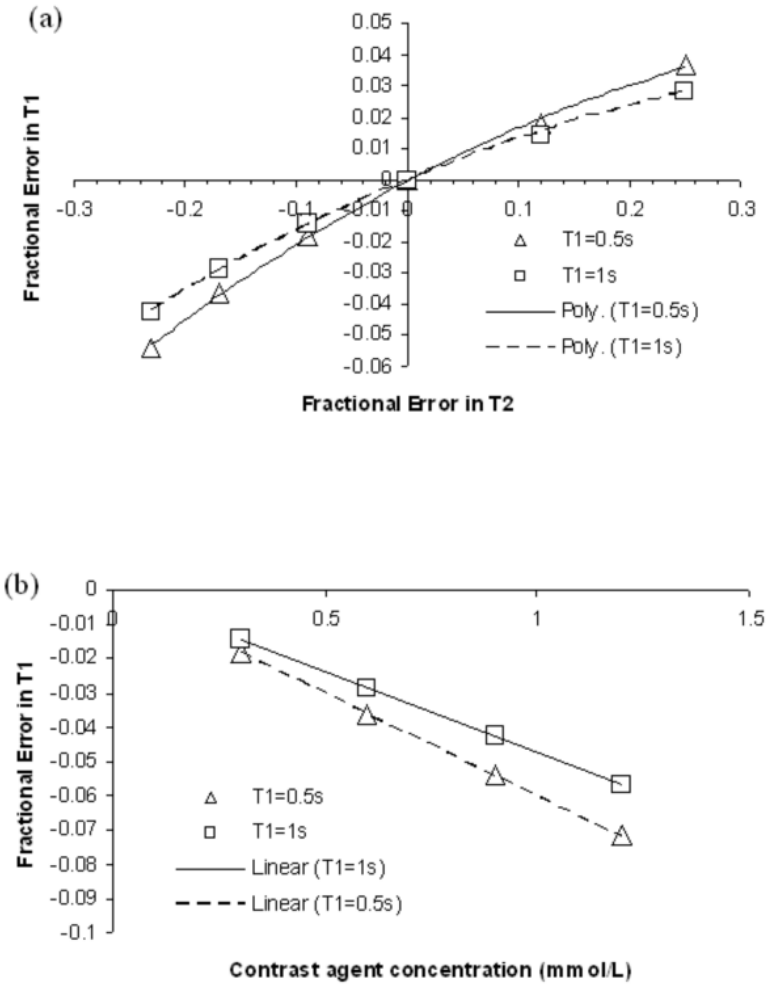

Figure 3.7. The computer simulation results of the fractional error in T_1 changes with (a) fractional error in T_2 and (b) local contrast agent concentration.

normal applications, 25% fractional error in T_2 induced less than 6% error on T_1-maps.

The signal recovery plots in Fig. 3.8 show the shortening of T_1 values at a point in the tumor periphery indicated by the vertical arrow in Fig. 3.9 at three time points after administration of contrast agent. The imaging duration for each time point was 15.0 s, during which data were measured for three different saturation recovery times τ_i.

The calculated T_1, T_2, and ΔR_1 maps are displayed in Fig. 3.9 for a central slice, and their values are plotted vs. time in Fig. 3.10 at selected 9 pixel regions of interest at the tumor periphery, the tumor core, and in muscle. No susceptibility induced distortion was noticeable on our dynamic T_1 measurement MR images. T_2 changes with contrast administration are negligible in this experiment, as presented in Figs. 3.9c and 3.10c. This is likely secondary to the low dose of 0.1 mM/kg of contrast agent used in this study. Phantom studies suggest that the T_2 shortening effect on the estimate of T_1 may become significant at higher contrast concentrations, which might be encountered in dynamic tumor imaging.

The dynamic change of ΔR_1 maps in Fig. 3.9b was calculated using T_1 maps and equation 3.5. These ΔR_1 images reflect the local distribution of the Gd[III] concentration. The temporal resolution using current technique may not be fast enough to accurately measure the arterial input function (AIF). The ΔR_1 images can be used to calculate the model-based pharmacokinetic

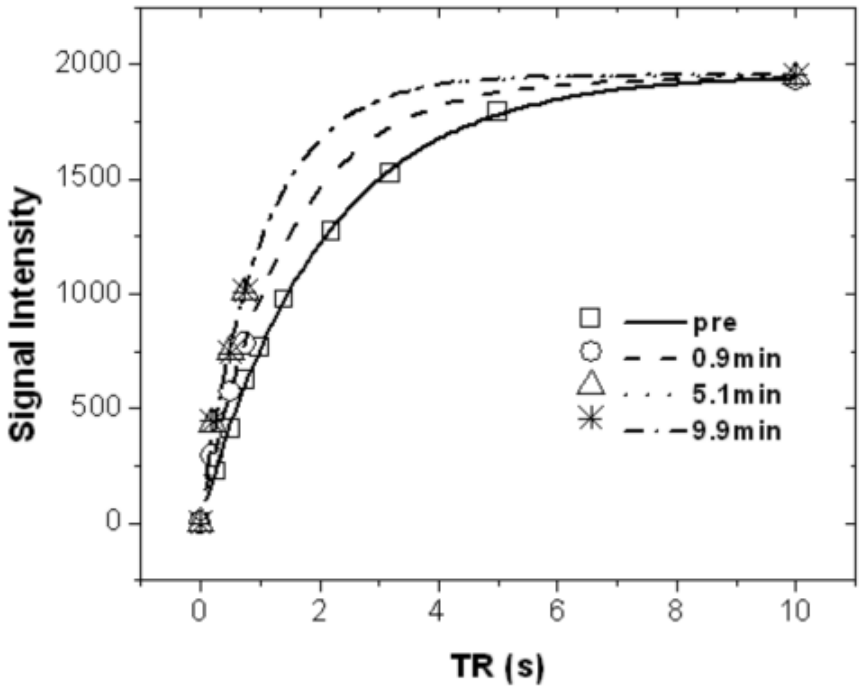

Figure 3.8. T_1 recovery curve of a single pixel near the tumor periphery that is indicated by the vertical arrow in Fig. 3.9a, at different dynamic time points.

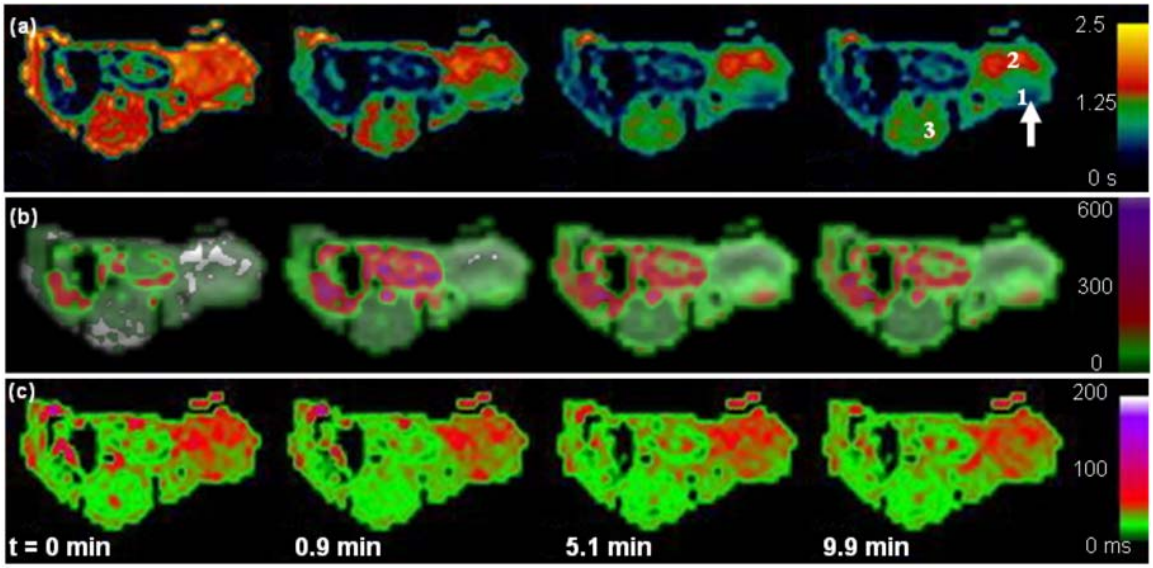

Figure 3.9. Figures of a) T_1 maps with T_2 correction, b) ΔR_1 maps, and c) T_2 maps at precontrast, and 0.9, 5.1, and 9.9 min after the bolus administration of Gd-DTPA. The blue end of the color map indicates lower T_1. Decreasing T_1, i.e., increasing ΔR_1, at the tumor periphery indicates increasing concentration of contrast agent. Average values at regions 1~3 are plotted in Fig. 3.10.

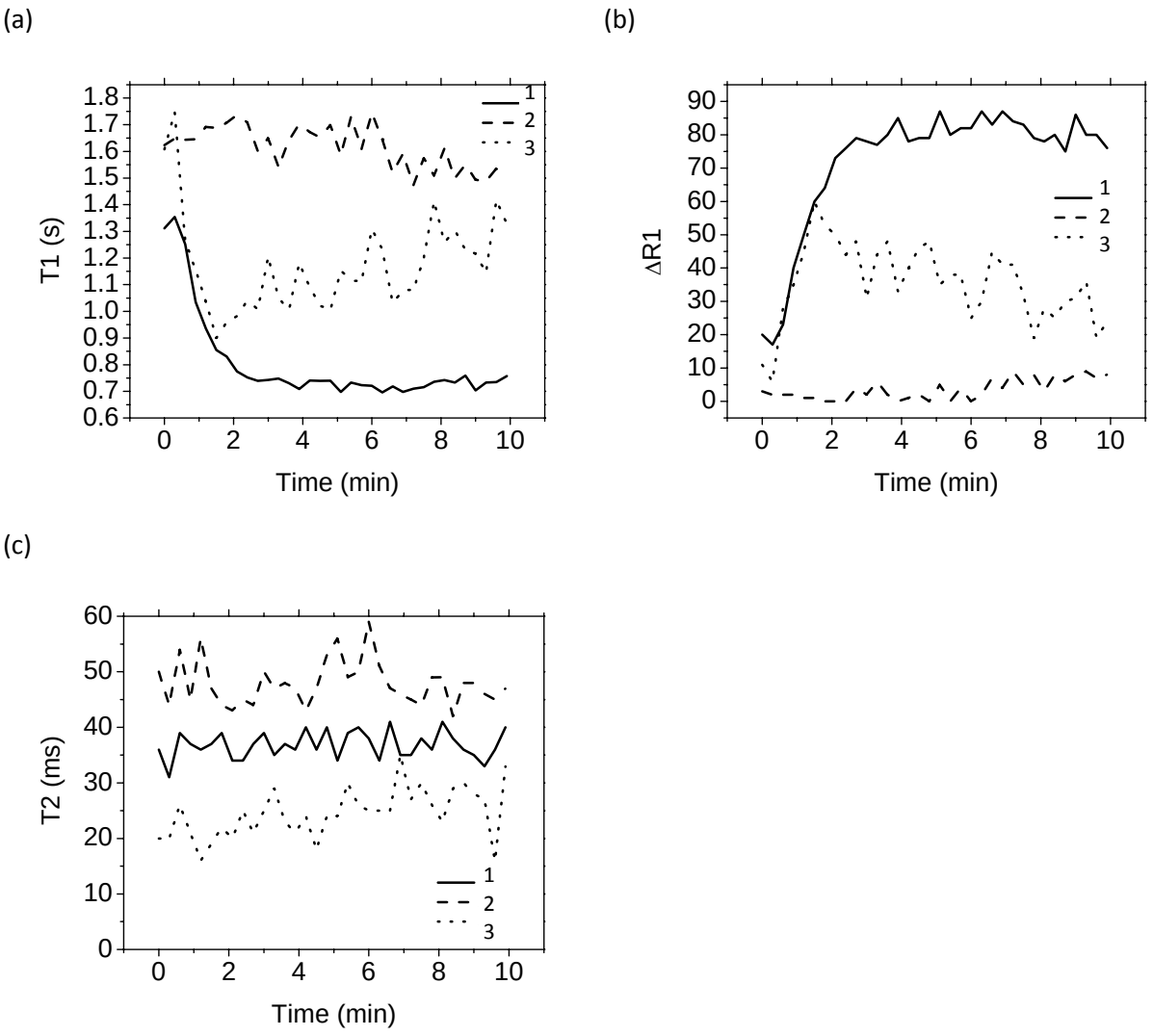

Figure 3.10. Plots of dynamic (a) T_1, (b) ΔR_1 and (c) T_2 values of 3x3 pixel regions of interest indicated by the numerals in Fig. 3.9.

parameters, such as blood perfusion and tissue permeability using certain models like reference region model (24) and Brix model (25-26) that do not require AIF. Although further research and validation of these ΔR_1 images are necessary for the absolute quantification, these ΔR_1 images may be considered as the close representation to the contrast concentration.

Phantom and *in vivo* studies show the accuracy and speed of the ms-DSEPI-T12 technique for T_1 and T_2 mapping. This method is much faster than conventional inversion-recovery sequences for T_1 mapping, and incurs little additional imaging time penalty for the addition of simultaneous T_2 mapping. Unlike the widely used technique of fast gradient echo imaging with flip angle variation, the T_1 estimates obtained by our method are insensitive to B_1 variation (20).

The multishot echo planar technique allows flexible tradeoff between imaging time and susceptibility effects such as geometric distortion. Longer echo train lengths lead to decreased imaging time and resulting improvement in time resolution of T_1 measurement, but also cause more severe artifacts from susceptibility. The increased echo trains may also result in underestimation of T_2.

The minimum recovery time is limited by the number of slices in current scheme, which may be erroneous to measure relatively short T_1 such as 100 ms. One solution is to acquire short TR images in two interleaved acquisitions. The temporal resolution can be further improved by sliding

window technique, which regroups the data set for T_1 map calculation. For instance, the data set with TRs [200, 500, 750], [200, 500,750] … can be grouped as [200, 500, 750], [500, 750, 200], [750, 200, 500], etc.

3.4 Conclusions

We have presented a rapid imaging method of simultaneous T_1 and T_2 mapping which is suitable for high temporal resolution measurement of T_1 for dynamic contrast enhanced MRI. Unlike conventional gradient recalled echo sequences with variable flip angle, this sequence is insensitive to B_1 inhomogeneity. Our method allows simultaneous measurement of T_2, which allows improved accuracy in T_1 measurement by compensating for T_2 effects. Accurate precontrast T_1 measurement in association with dynamic T_2 measurement also allows more rapid post-contrast T_1 measurement by reducing the number of saturation recovery time points necessary for accurate T_1 recovery curve fitting. Resulting T_1 measurements agree experimentally with results obtained by slower inversion-recovery methods, with a fraction of the imaging time. Preliminary experiments in mice show that this method may be useful in dynamic contrast concentration MR imaging which may depict the distribution and pharmacokinetics of contrast agents or gadolinium-labeled pharmaceuticals.

3.5 Acknowledgements

This work was partly supported by University of Utah VP Seed Grant, and NIH Grants R01CA097465 and 1R01EY015181.

3.6 References

1. Erlemann R, Reiser MF, Peters PE, et al. Musculoskeletal neoplasms: static and dynamic Gd-DTPA--enhanced MR imaging. Radiology 1989;171(3):767-773.

2. Carr DH, Brown J, Bydder GM, et al. Gadolinium-DTPA as a contrast agent in MRI: initial clinical experience in 20 patients. AJR 1984;143(2):215-224.

3. Saini S, Stark DD, Brady TJ, Wittenberg J, Ferrucci JT, Jr. Dynamic spin-echo MRI of liver cancer using Gadolinium-DTPA: animal investigation. AJR 1986;147(2):357-362.

4. Krestin GP, Steinbrich W, Friedmann G. Adrenal masses: evaluation with fast gradient-echo MR imaging and Gd-DTPA-enhanced dynamic studies. Radiology 1989;171(3):675-680.

5. Vogl T, Bruning R, Schedel H, et al. Paragangliomas of the jugular bulb and carotid body: MR imaging with short sequences and Gd-DTPA enhancement. AJR 1989;153(3):583-587.

6. Hamm B, Fischer E, Taupitz M. Differentiation of hepatic hemangiomas from metastases by dynamic contrast-enhanced MR imaging. Journal of Computer Assisted Tomography 1990;14(2):205-216.

7. Krestin GP, Lorenz R, Steinbrich W. [Magnetic resonance tomography of adrenal gland tumors. Detection and differentiation using fast gradient echo sequences and dynamic contrast media studies]. Der Radiologe 1990;30(5):228-234.

8. Stack JP, Redmond OM, Codd MB, Dervan PA, Ennis JT. Breast disease: tissue characterization with Gd-DTPA enhancement profiles. Radiology 1990;174(2):491-494.

9. Demsar F, Roberts TP, Schwickert HC, et al. A MRI spatial mapping technique for microvascular permeability and tissue blood volume based on macromolecular contrast agent distribution. Magn Reson Med 1997;37(2):236-242.

10. Buckley DL, Drew PJ, Mussurakis S, Monson JR, Horsman A. Microvessel density of invasive breast cancer assessed by dynamic Gd-DTPA enhanced MRI. J Magn Reson Imaging 1997;7(3):461-464.

11. Bloembergen N, Purcell EM, Pound RV. Relaxation Effects in Nuclear Magnetic Resonance Absorption. Physical Review 1948;73(7):679-712.

12. Solomon I. Relaxation processes in a system of two spins. Physical Review 1955;99(2):559-565.

13. Bloembergen N. Proton Relaxation Times in Paramagnetic Solutions. Journal of Chemical Physics 1957;27:572-573.

14. Tofts P. Quantitative MRI of the Brain: Measuring Changes Caused By Disease. Chichester, West Sussex ; Hoboken, N.J.: Wiley; 2003.

15. Folkman J. What is the evidence that tumors are angiogenesis dependent? Journal of the National Cancer Institute 1990;82(1):4-6.

16. Look DC, Locker DR. Time Saving in Measurement of NMR and EPR Relaxation Times. Review of Scientific Instruments 1970;41(2):2.

17. Gowland P, Mansfield P. Accurate measurement of T1 in vivo in less than 3 seconds using echo-planar imaging. Magn Reson Med 1993;30(3):351-354.

18. Farzaneh F, Riederer SJ, Pelc NJ. Analysis of T2 limitations and off-resonance effects on spatial resolution and artifacts in echo-planar imaging. Magn Reson Med 1990;14(1):123-139.

19. Cohen MS, Weisskoff RM. Ultra-fast imaging. Magnetic Resonance Imaging 1991;9(1):1-37.

20. Deoni SC, Rutt BK, Peters TM. Rapid combined T1 and T2 mapping using gradient recalled acquisition in the steady state. Magn Reson Med 2003;49(3):515-526.

21. Liu X, Feng Y, Ke T, et al. Rapid Data Acquisition for T1 Mapping, Using Multishot EPI and Automated TR Variation at 3T. ISMRM. Seattle, Washington, USA; 2006. p. 2500.

22. Liu X, Feng Y, Lu ZR, Jeong EK. Rapid Simultaneous Data acquisition of T1 and T2 Mapping, Using Multishot EPI and Automated Variations of TR and TE at 3T. ISMRM. Berlin, Germany; 2007. p. 5617.

23. Slichter CP. Principles of Magnetic Resonance. Berlin, Germany: Springer-Verlag: 1990.

24. Yankeelov TE, Luci JJ, Lepage M, et al. Quantitative pharmacokinetic analysis of DCE-MRI data without an arterial input function: a

reference region model. Magnetic Resonance Imaging 2005;23(4):519-529.

25. Brix G, Bahner ML, Hoffmann U, Horvath A, Schreiber W. Regional blood flow, capillary permeability, and compartmental volumes: measurement with dynamic CT--initial experience. Radiology 1999;210(1):269-276.

26. Brix G, Kiessling F, Lucht R, et al. Microcirculation and microvasculature in breast tumors: pharmacokinetic analysis of dynamic MR image series. Magn Reson Med 2004;52(2):420-429.

CHAPTER 4

OCULAR PHARMACOKINETICS STUDY OF A CORTICOSTEROID BY ^{19}F MR

This chapter is based on the paper "Ocular pharmacokinetics study of a corticosteroid by ^{19}F MR," which was published on the journal Experimental Eye Research in 2010, authored by Xin Liu, S. Kevin Li and Eun-Kee Jeong.

4.1 Introduction

Corticosteroids such as triamcinolone acetonide (TA) and dexamethasone sodium phosphate (DSP) have been widely used in the treatment of macular edema and uveitis (1-2). Intravitreal injection is an efficient way to deliver corticosteroid to the back of the eye to avoid systemic side effects. However, the intravitreal treatment is often short-lived, and repeated administration is usually required for chronic diseases (1). Information on how long the drug will stay in the eye after the initial injection and the clearance of the drug after the injection is of significance that can help healthcare practitioners understand the duration of the therapeutic effect and modify the dosing regimen for effective therapy.

Conventional pharmacokinetics studies with animals require sacrificing the animals at different time points after drug administration, dissecting the eye, and analyzing different sections of the eye for the drug. The concentration of the drug in the eye tissues will then be determined using assays such as high-performance liquid chromatography (HPLC). However, this method is not applicable to humans. In human ocular pharmacokinetic studies, samples in the vitreous humor and anterior chamber could be extracted in conjunction with surgical procedures such as cataract surgery or vitrectomy (3-4), but the amount of the drug in the eye or in eye tissues cannot be measured accurately and can only be estimated. The lack of human pharmacokinetic data in ocular drug delivery research has hindered its development and the advance of ocular drug delivery technologies. A noninvasive approach to study ocular pharmacokinetics and drug clearance in the eye, e.g., after intravitreal injections, cannot only reduce the number of animals required in ocular drug delivery and pharmacokinetic research, but also allow the determination of the concentration profiles in the eye on a real time basis. Such methods may also be applicable to humans in clinical studies.

The objective of the present study was to develop a noninvasive way using ^{19}F MR on a 3T clinical scanner to study ocular pharmacokinetics of fluorine containing therapeutic agents. Particularly, the real time pharmacokinetics of intraocular triamcinolone acetonide phosphate (TAP)

was monitored after intravitreal injection. TAP is a prodrug of TA and has higher water solubility than TA (Fig. 4.1). The molecular weight of TAP is close to that of TA and DSP. Since the molecular structures of TAP and DSP are similar, the diffusion coefficient of TAP in the vitreous humor is expected to be similar to that of DSP, making TAP a useful surrogate to study the behavior of DSP clearance in the eye.

4.2 Materials and Methods

4.2.1 Materials

TAP dipotassium salt was purchased from Crystal Pharma (Valladolid, Spain). TAP 0.09 M was prepared by dissolving TAP powder in deionized water. $MnCl_2$ tetrahydrate was obtained from Spectrum Chemical (Gardena, CA). Ethylenediamine tetraacetic acid (EDTA) and xylazine were acquired from Sigma Chemical (St. Louis, MO). $Na_2MnEDTA$ solutions (0.02 M) were prepared by mixing $MnCl_2$ with EDTA in deionized water and adjusting the pH of the solution to 7 with concentrated NaOH.

4.2.2 Animals

New Zealand white rabbits of 3 to 4 kg body-weight were purchased from Western Oregon Rabbit Co. (Philomath, OR). Animal experiments were conducted with the approval of the Institutional Animal Care and Use Committee at the University of Utah.

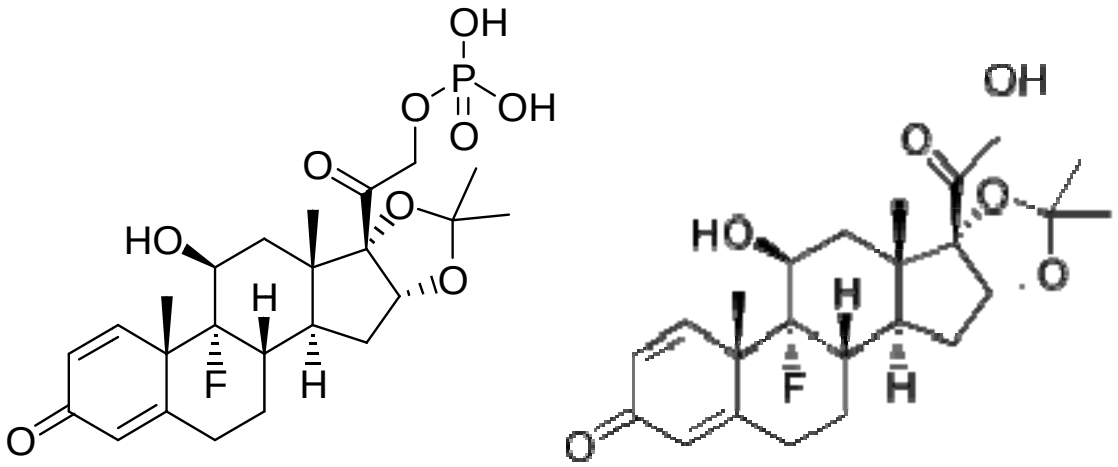

Figure 4.1. Molecular structures of triamcinolone acetonide phosphate (left) and triamcinolone acetonide (right).

4.2.3 Animal Experiments

Rabbits were anesthetized by intramuscular injection of 25 to 50 mg/kg ketamine and 5 to 10 mg/kg xylazine. The rabbits were then given either intravitreal or subconjunctival injections of 0.1 mL 0.09 M TAP mixed with approximately 1 μmol of Na_2MnEDTA (MnEDTA ion). In postmortem rabbit studies, rabbits were sacrificed immediately before TAP injection. A total of 12 eyes were used for intravitreal injection: 6 eyes of 3 rabbits *in vivo* and 6 eyes of 3 rabbits postmortem; 6 eyes were used for subconjunctival injection: 3 eyes of 2 rabbits (the other eye was used for other purposes, e.g., a control) *in vivo* and 3 eyes of 2 rabbits postmortem. ^{19}F spectra were obtained at different time points after the injection. To determine the injection spot, MnEDTA ion was monitored with T_1-weighted ^{1}H imaging. ^{1}H MRI was taken before and at the time points after the injections.

4.2.4 MRI

All MRI experiments were performed on a Siemens 3T Trio clinical imaging system (Siemens Medical Solution, Erlangen, Germany). Because most of the clinical scanners do not have commercial ^{19}F coils and coil-to-scanner interface, a purpose-built circular linear surface coil with 1.5 inch diameter was tuned to 115.93 MHz to transmit the excitation pulse and receive the ^{19}F NMR signal. A similar coil with the same dimension was tuned to 123.22 MHz to acquire ^{1}H anatomy images. The coil assembly consisted of an RF resonator, T/R switch, preamplifier, and the coil-plug. In

this experiment, surface coils were used to improve the signal detection sensitivity. The 1.5 inch diameter coil allowed the rabbit eye to slightly protrude out of the coil plane, which made the eyeball sit symmetrically about the coil plane. This was to position the eyeball in the most sensitive region of the coil. Since the surface coil field penetration depth was about same as the size as the coil, a coil diameter of 1.5 inches ensured that the sensitivity region of the coil covered deep enough for the eyeball. Active T/R switching with PIN diodes and a quarter-wave (λ/4) coaxial cable were used to switch between transmit and receive modes of the coil assembly. The same λ/4 was used for both proton and ^{19}F channels. A 3-200 MHz broadband preamplifier was used to amplify the received MR signals. A small vial of KF solution was attached to the ^{19}F coil to generate a reference signal to calibrate the signal difference caused by coil loading variation.

A dynamic ^{19}F spectrum was obtained with a free induction decay (FID) pulse sequence: 1 s repetition time (TR), 0.15 ms receiver delay time, 16 kHz receiver bandwidth, 90° flip angle, 256 averages, and vector size of 1024. The data acquisition time was 4 min 20 sec. A rectangular (hard) RF pulse was used with a 200 μs pulse width. The irradiation bandwidth (~10 kHz) covered both TAP and KF peaks (the two peaks were about 4-5 kHz apart on our 3T scanner). The NMR data were acquired at various time points after the intravitreal and subconjunctival injections as described in the "Animal

Experiment" section. For some rabbits, multiple measurements were taken at the same time points.

High-resolution ^{1}H images were acquired using a gradient recall echo (GRE) pulse sequence: field of view (FOV) 108 mm, 50% phase-FOV, spatial resolution 0.34×0.34×1.5 mm^3, 20 slices, TR 400 ms, echo time (TE) 4.28 ms, 400 Hz/pixel bandwidth, 2 averages, 60° flip angle, and acquisition time 2 min 10 sec.

The T_1 of intravitreal TAP was also obtained during the experiment to determine if there was any T_1 change with decrease of TAP concentration. FID pulse sequences were used to acquire T_1 weighted spectra: 0.15 ms receiver delay time, 16 kHz bandwidth, 90° flip angle and 256 averages, repetition times were 200, 400, 800, 1600 and 3200 ms.

4.2.5 MR Data Processing

All ^{19}F spectra were processed by custom-programmed MR spectroscopy analysis software developed using IDL (Interactive Data Language, ITT Visual Software, Boulder, CO). 10 Hz Gaussian apodization was applied in the time domain, followed by baseline correction, Fourier-transformation, and phase-correction. The peak area integrations for both TAP and KF NMR lines were performed within the software. Ratios of the KF peak area to the TAP peak area at all time points were calculated then multiplied by TAP peak areas at each corresponding time point to create TAP signals with consistent coil sensitivity, i.e., normalized TAP signals. For each

rabbit eye, the relative TAP signals were calculated as ratios of the normalized TAP signals at different time points to the normalized TAP signal at the initial time point.

4.3 Results

4.3.1 Intravitreal and Subconjunctival Injections

A typical ^{19}F spectrum of TAP and KF obtained from our experiments is shown in Fig. 4.2a. The separation of two peaks is about 47 ppm, which is about 5.5 kHz on the 3T scanner. Fig. 4.2b shows the ^{19}F spectra of a representative rabbit eye *in vivo* at different time points after intravitreal injection, where all spectra have been normalized to the KF spectrum. The data show the change in the spectrum over time throughout the experiment (from 0 to 22 hours). The TAP peaks maintained similar shapes and widths while the height decreased over time to the level of noise after 22 hours (the upper right spectrum). The signal-to-noise ratio (SNR) of the spectrum at the initial time point in the experiments ranges from 50 to 80.

The ^{1}H MR images of the same eye are shown in Fig. 4.3, immediately before, immediately after, and 5 hours after the intravitreal injection. The MR images of MnEDTA show the site of the injection. The injection spot was close to the center of the vitreous body, and the solution immediately spread in both directions to the retina and the back of the lens. The images also show that the shape of the injection spot in the vitreous was not entirely spherical and MnEDTA spread behind the lens. The spreading suggests a

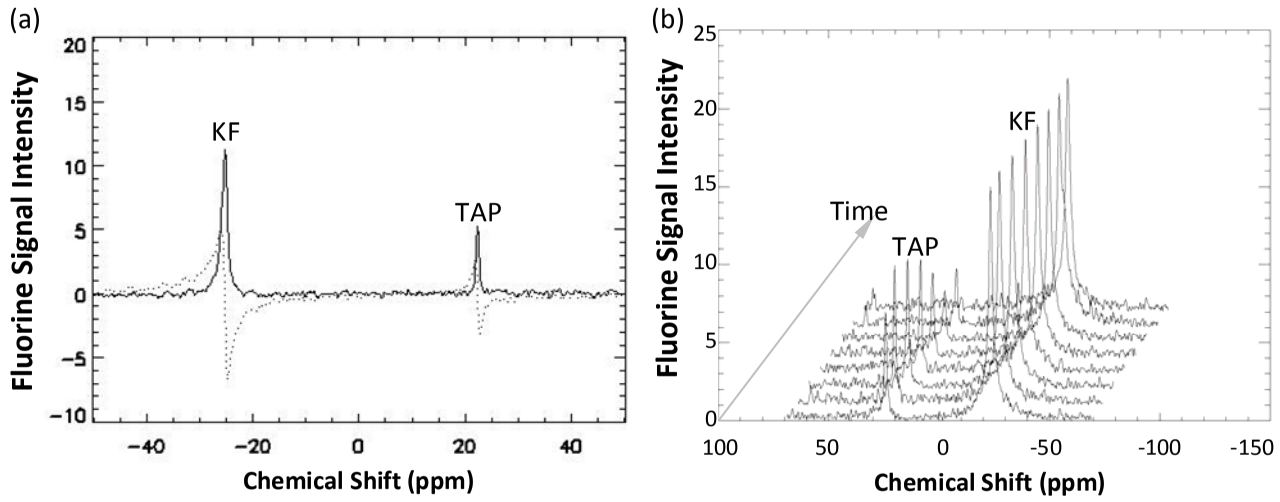

Figure 4.2. Representative ^{19}F spectra at (a) one time point and (b) different time points obtained in a rabbit *in vivo*, where all spectra have been normalized according to the KF spectrum. In (b), the time axis is not spaced according to the time scale.

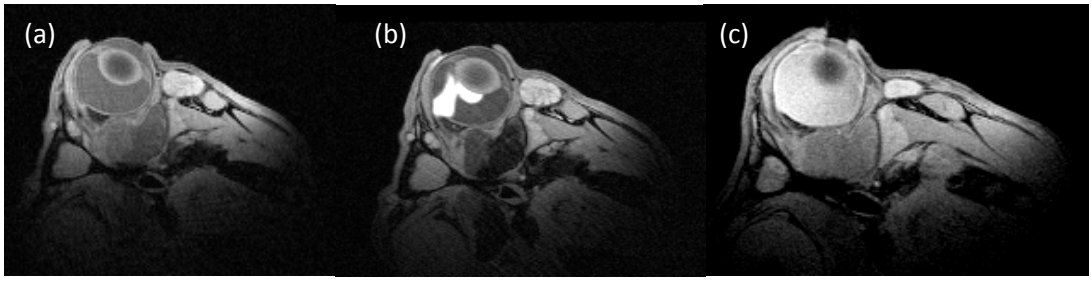

Figure 4.3. ^{1}H MR images (a) right before, (b) immediately and (c) 5 hours after the intravitreal injection. The bright region in (b) indicates the initial location of the TAP/MnEDTA/saline solution.

less resistive region behind the lens to the flow of the solution introduced by the needle during the injection. At 5 hours after the injection, MnEDTA had spread throughout the vitreous body and other parts of the eye. In addition to showing the location of the intravitreal injection, the MnEDTA data also provided information on the diffusion pattern of TAP since MnEDTA and TAP have similar molecular weights (~386 and 529 Dalton, respectively) and are expected to have similar diffusion coefficients.

Fig. 4.4 presents the amount of TAP at different time points after the intravitreal injection *in vivo* (6 eyes) and postmortem (6 eyes). Fig. 4.5 shows the amount of TAP at different time points after the subconjunctival injection *in vivo* (3 eyes) and postmortem (3 eyes). The data of each eye were fit into a first order clearance model to determine the elimination half-life ($t_{1/2}$) of the TAP signal in each experiment using the first order exponential function:

$$A = A_0 \times \exp(-k_{obs}t) \quad \ldots.(4.1)$$

where A is the signal (proportional to the drug concentration), A_0 is the initial signal, k_{obs} is the rate constant, and t is time. The average elimination half-life $t_{1/2}$ was calculated and is presented in Table 4.1.

4.3.2 ^{19}F T_1 Measurement of Intraocular TAP

The MR signal intensity follows an exponential recovery equation:

$$S = S_0 \times [1 - \exp(-TR/T_1)] \quad \ldots.(4.2)$$

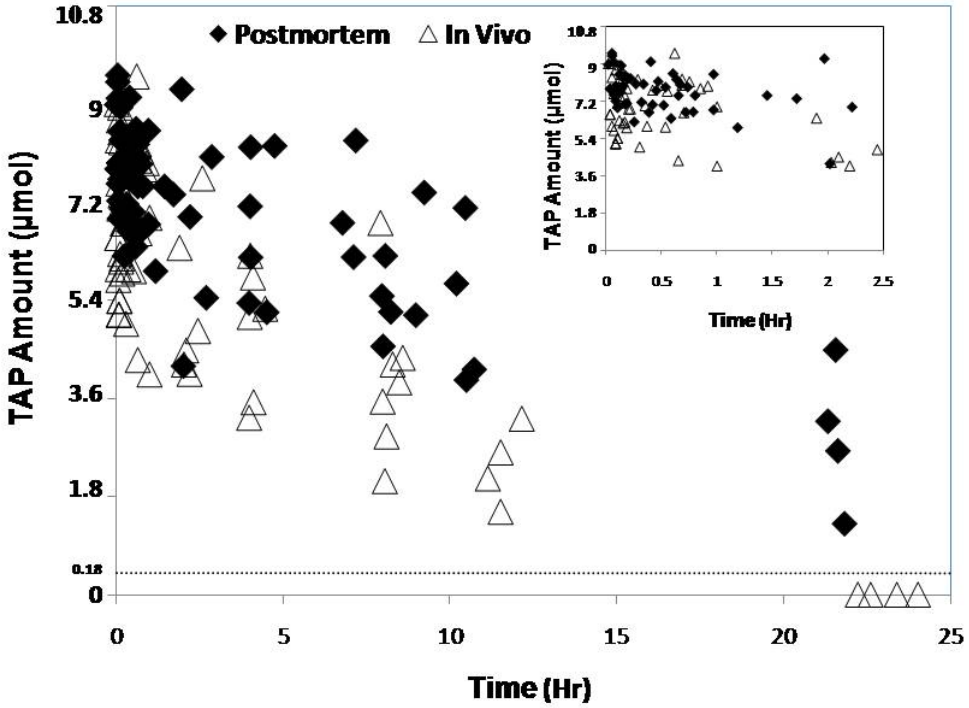

Figure 4.4. Relative TAP signal versus time after intravitreal injection *in vivo* and postmortem. The insert shows an enlarged view of the data. The line indicates the detection limit with the coil and pulse sequence used in this study.

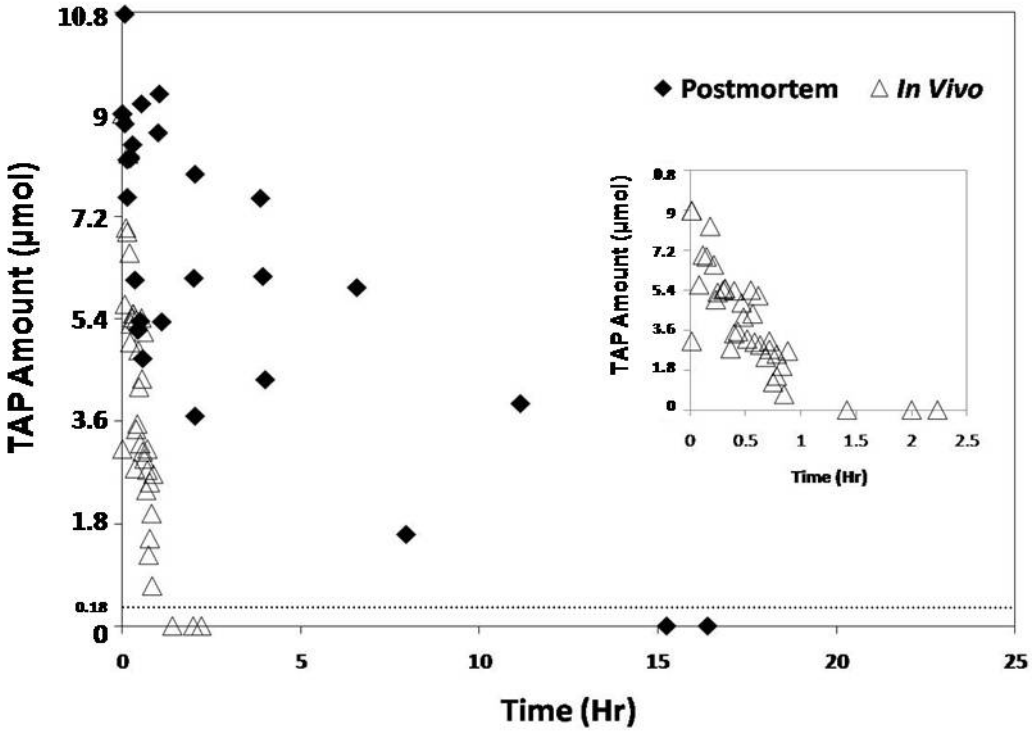

Figure 4.5. Relative TAP signal versus time after subconjunctival injection *in vivo* and postmortem. The insert shows an enlarged view of the *in vivo* data. The line indicates the detection limit with the coil and pulse sequence used in this study.

Table 4.1. Summary of the first order rate constant and elimination half life[a].

	k_{obs} (h^{-1})	$t_{1/2}$ (h)
Intravitreal injection *in vivo*	0.09±0.02	7.8±1.1
Intravitreal injection postmortem	0.04±0.01	17.2±2.1
Subconjunctival injection *in vivo*	1.4±0.2	0.5±0.1
Subconjunctival injection postmortem	0.11±0.03	6.0±1.5

[a] Mean±SD (n=3 for subconjunctival injection; n=6 for intravitreal injection).

where S and S_0 are the transient and the equilibrium signal intensities, respectively. With a fixed TR, T_1 change will affect the signal intensity. ^{19}F T_1 was measured as 907±165 ms and 883±370 ms at 20 minutes and 4 hours after the intravitreal injection, respectively. The ^{19}F T_1 values of TAP were essentially the same that indicates negligible effect on the ^{19}F signal intensity during the experiment. In the subconjunctival injection experiments, the TAP signal decayed quickly and T_1 measurements were not performed.

4.4 Discussion

4.4.1 Ocular Clearance

Drugs delivered through intravitreal injections can be eliminated through the aqueous humor outflow pathways in the anterior of the eye such as the canal of Schlemm or across the retinal/choroidal layer surrounding the vitreous (5-6). For small molecules, the predominant route of clearance is suggested to be through the retina in the posterior segment of the eye (7). The diffusion of a drug in the vitreous mainly depends on its molecular weight (or molecular size), and permeation across the retina depends on the lipophilicity of the drug. Therefore, clearance from the vitreous, e.g., after intravitreal injections, generally depends on the molecular weight, lipophilicity, and charge of the molecule. These factors also determine if clearance is diffusion or barrier controlled. Small lipophilic molecules usually have faster clearance than charged molecules provided that binding to ocular tissues is not important. For example, the terminal half-lives of small

molecules in the vitreous in rabbits can range from 3-4 h for the corticosteroid dexamethasone (8-9), to 5 h for the antibiotic carbenicillin (10) and to greater than 12 h for the antiviral foscarnet (11) that is used in the treatment of herpes and cytomegalovirus. Whereas dexamethasone is lipophilic and uncharged having a molecular weight of 392 Daltons, carbenicillin and foscarnet are charged (2-, and 3-, respectively) with molecular weights of 378 and 126 Dalton, respectively. The half-life of third-generation cephalosporins in the vitreous humor ranges from 5-20 h (12). In the present study, TAP, a charged molecule of 515 Dalton, had a half-life of 8 h after intravitreal injection, which is consistent with the range provided in the literature. Clearance from the subconjunctival pocket and anterior chamber after subconjunctival injection is generally fast compared with that from the vitreous. In general, the half-lives of molecules in the subconjunctival pocket are approximately 0.3-0.5 h after subconjunctival injection(13-14). Half-lives for clearance from the anterior chamber are less than 1 h for pilocarpine (15) and methazolamide (16) and up to 2 h for dorzolamide (17). The TAP result after subconjunctival injection in the present study is in the same order of magnitude as those in the literature (18-19). Clearance of intravitreal injection of drugs in suspension form is generally much slower than water soluble drugs. Half-life of triamcinolone acetonide clearance from vitreous, for example, is 5-6 days (20).

TAP can be a surrogate to study ocular pharmacokinetics of therapeutic agents of similar physiochemical properties (molecular size and charge) and understand the mechanism of clearance after intravitreal and subconjunctival injections. For example, TAP and DSP have similar molecular weights, and if the clearance is diffusion controlled after intravitreal administration, the behavior of TAP clearance will be similar to that of DSP.

4.4.2 Intravitreal and Subconjunctival Injections

The present results show that the TAP signal decays at a much higher rate after subconjunctival injection *in vivo* than after intravitreal injection *in vivo* (1.4 vs. 0.09 h^{-1}). This is consistent with the mechanisms of ocular clearance and the pharmacokinetic profiles observed after subconjunctival and intravitreal injections in the literature (18-19). A major difference between the routes of ocular clearance after subconjunctival injection versus intravitreal injection *in vivo* is the distance for TAP to reach the clearance site such as the blood vasculature in the choroid and retina or to reach the anterior chamber and the Schlemm's canal. Following subconjunctival injection, TAP is in direct contact with the blood vasculature in the surrounding tissues of the subconjunctival space. Clearance of TAP after intravitreal injection requires diffusion across the vitreous humor before it can be cleared from the eye.

4.4.3 *In Vivo* and Postmortem Studies

If euthanasia compromised the tissue barriers in the eye, an increase in TAP clearance was expected postmortem. On the other hand, if clearance was the dominant factor, a decrease in TAP clearance was expected due to the lack of a functional vasculature around the eyes postmortem. The present data show significantly slower clearance of TAP from the eye in the postmortem animals compared with those *in vivo*: 0.04 vs. 0.09 h^{-1} for postmortem and *in vivo* after intravitreal injection, and 0.11 vs. 1.4 h^{-1} for postmortem and *in vivo* after subconjunctival injection, respectively. This is consistent with blood circulation around the eyes being a dominant factor for the decrease in the TAP signal. Although the blood retina barrier became compromised after animal death (21), an assumption that the tissues in the eye such as the choroid, retina, and endothelial cell tight junctions remained functionally and structurally intact postmortem (22) was made as a first approximation in the analysis. Under this assumption, the effect of clearance through the blood vasculature could be estimated by the following pharmacokinetic model:

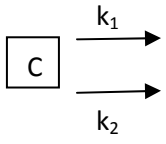

$$\frac{dC}{dt} = -(k_1 + k_2)C \quad \ldots . (4.3)$$

where k_1 is the rate constant of TAP clearance from the eye due to blood vasculature and other factors that cease at the death of the animal and k_2 is the rate constant due to clearance such as passive diffusion and other factors in the animal postmortem. Accordingly, k_2 equals the rate constant of TAP observed postmortem and the sum $k_1 + k_2$ equals the apparent rate constant k_{obs} of clearance *in vivo*. A comparison of the *in vivo* and postmortem results shows that the rate constants k_1 for TAP (e.g., blood vasculature clearance) are 0.05 and 1.3 h^{-1} after intravitreal and subconjunctival administrations, respectively. This corresponds to the termination half-life due to clearance of 14 hr for intravitreal injection and 0.5 hr for subconjunctival injection.

4.4.4 Other Considerations

It has been suggested that the position of the intravitreal injection is important for drug distribution and elimination in the eye (23-24). For example, when the site of injection for intravitreal delivery is at the center of the vitreous body and the TAP solution injected maintains a spherical shape, TAP would diffuse isotropically and then be cleared by blood vasculature at the retina. This scenario would result in the slowest clearance due to the diffusion that needs to take place. However, as shown in Fig. 4.3 in the present study, MnEDTA had already reached the retina soon after the intravitreal injection. The problem is possibly caused by the relatively large amount of TAP solution (0.1 mL) injected, compared to the volume of the rabbit vitreous humor (0.7 ~ 1.5 mL). This would increase the clearance rate

of TAP after the injection and introduce variability in intravitreal injection in general.

MnEDTA has been used in MRI and shows low toxicity at low concentration. In our experiments the concentration of MnEDTA solution injected is low. Therefore, it is unlikely that MnEDTA has retinal toxicity in our case and presence of MnEDTA would not affect the pharmacokinetics of TAP.

Other factors that might contribute to the signal decrease include the degradation of TAP to TA in the eye, an inhomogeneous RF field distribution, and the change in T_1 of TAP in different eye compartments or change of T1 by some factors, e.g., partial pressure of oxygen. The first explanation is based on the low solubility of TA in the vitreous humor; the aqueous solubility of TA is approximately 0.036 mg/mL (25) although a previous study has shown that the aqueous concentration of TA in the vitreous is 0.7 mg/mL (26) possibly due to TA interactions with the vitreous humor components. TA in solid state is expected to have a short T_2 so the signal would decrease significantly when TAP is converted to TA and subsequently precipitated in the vitreous. However, this cannot explain the different results observed in the *in vivo* and postmortem experiments. The second explanation is related to coil signal inhomogeneity, in which TAP might diffuse to the places in the eye with less coil sensitivity. Again, if this were the major reason for the decrease in the TAP signal, the *in vivo* and postmortem experiments would not show

different results. The last explanation was found to be unlikely because T_1 measurements have shown similar T_1 values (907 vs. 883 ms, respectively) at 20 minutes and 4 hr after the injection.

4.4.5 Detection and Limitations

There are limitations using rabbits as an animal model to study pharmacokinetics at the back of the eye and extrapolate the results to human because the eyes such as the inner retinal blood circulations in rabbits and human are dissimilar. The goal of the present study is to eventual apply this technique on human in the future. To use ^{19}F MR to study ocular pharmacokinetics in human, some technical issues remain to be addressed. Particularly, the ^{19}F MR method has relatively low sensitivity compared to traditional assay techniques (e.g., HPLC and GC). The detection limit of ^{19}F MR for TAP was about 0.18 μmol with the current RF coil and setup. When the TAP amount was less than 0.18 μmol in the eye, the signal was below noise level (about 2% of the 9 μmol initial total amount of the TAP injected). Although the SNR of the spectrum at the initial time points was 50-80 and provided sufficient detection in the present intravitreal and subconjunctival injection study, this detection limit may not be sensitive enough for ocular pharmacokinetic studies to evaluate other ocular drug delivery methods. Further hardware improvement or pulse sequence modification is required to increase the detection limit.

4.5 Conclusion

A whole-body clinical MRI system was modified to perform ^{19}F MR with a FID pulse sequence for noninvasive ocular pharmacokinetic studies. Ocular pharmacokinetic experiments were conducted using triamcinolone acetonide phosphate (TAP) as the model drug in rabbits *in vivo* and postmortem. The apparent elimination rate constants and half-lives of TAP in the eye after drug administration were determined. The difference in clearance observed *in vivo* and postmortem suggests the importance of fluid dynamics in the eye and blood circulation around the eyes to TAP clearance. The rate constants related to such clearance were then calculated. The higher clearance after subconjunctival injection relative to that of intravitreal injection was believed to be due to the distance of the injection site from the blood vasculature. Finally, the present study demonstrates the feasibility of noninvasively monitoring the clearance of fluorine-containing drugs after ocular delivery using ^{19}F MR, which may allow the eventual use of this method to study ocular pharmacokinetics in human.

4.6 Acknowledgements

This research was supported by NIH Grant EY15181. The authors thank Dr. Sarah A. Molokhia for her help in some experiments and Dr. Roy Rowley for his careful review of the wording and grammar in this paper.

4.7 References

1. Kiernan DF, Mieler WF. The use of intraocular corticosteroids. Expert Opin Pharmacother 2009;10(15):2511-2525.

2. Yilmaz T, Weaver CD, Gallagher MJ, et al. Intravitreal triamcinolone acetonide injection for treatment of refractory diabetic macular edema: a systematic review. Ophthalmology 2009;116(5):902-911; quiz 912-903.

3. Cheng L, Banker AS, Martin M, Kozak I, Freeman WR. Triamcinolone acetonide concentration of aqueous humor after decanted 20-mg intravitreal injection. Ophthalmology 2009;116(7):1356-1359.

4. Zaka-ur-Rab S, Mahmood S, Shukla M, Zakir SM, Khan BA, Owais M. Systemic absorption of triamcinolone acetonide after posterior sub-Tenon injection. Am J Ophthalmol 2009;148(3):414-419.

5. Maurice D. Review: practical issues in intravitreal drug delivery. J Ocul Pharmacol Ther 2001;17(4):393-401.

6. Urtti A. Challenges and obstacles of ocular pharmacokinetics and drug delivery. Adv Drug Deliv Rev 2006;58(11):1131-1135.

7. Worakul N, Robinson JR. Ocular pharmacokinetics/pharmacodynamics. Eur J Pharm Biopharm 1997;44:71-83.

8. Graham RO, Peyman GA. Intravitreal injection of dexamethasone. Treatment of experimentally induced endophthalmitis. Arch Ophthalmol 1974;92(2):149-154.

9. Kwak HW, D'Amico DJ. Evaluation of the retinal toxicity and pharmacokinetics of dexamethasone after intravitreal injection. Arch Ophthalmol 1992;110(2):259-266.

10. Barza M, Kane A, Baum J. The effects of infection and probenecid on the transport of carbenicillin from the rabbit vitreous humor. Invest Ophthalmol Vis Sci 1982;22(6):720-726.

11. Berthe P, Baudouin C, Garraffo R, Hofmann P, Taburet AM, Lapalus P. Toxicologic and pharmacokinetic analysis of intravitreal injections of foscarnet, either alone or in combination with ganciclovir. Invest Ophthalmol Vis Sci 1994;35(3):1038-1045.

12. Barza M, Lynch E, Baum JL. Pharmacokinetics of newer cephalosporins after subconjunctival and intravitreal injection in rabbits. Arch Ophthalmol 1993;111(1):121-125.

13. Kim SH, Csaky KG, Wang NS, Lutz RJ. Drug elimination kinetics following subconjunctival injection using dynamic contrast-enhanced magnetic resonance imaging. Pharm Res 2008;25(3):512-520.

14. Li SK, Molokhia SA, Jeong EK. Assessment of subconjunctival delivery with model ionic permeants and magnetic resonance imaging. Pharm Res 2004;21(12):2175-2184.

15. Lee vHL, Robinson JR. Disposition of pilocarpine in the pigmented rabbit eye. Int J Pharm 1982;11:155-165.

16. Maren TH, Jankowska L. Ocular pharmacology of sulfonamides: the cornea as barrier and depot. Curr Eye Res 1985;4(4):399-408.

17. Sugrue MF. The preclinical pharmacology of dorzolamide hydrochloride, a topical carbonic anhydrase inhibitor. J Ocul Pharmacol Ther 1996;12(3):363-376.

18. Lee TW, Robinson JR. Drug delivery to the posterior segment of the eye II: development and validation of a simple pharmacokinetic model for subconjunctival injection. J Ocul Pharmacol Ther 2004;20(1):43-53.

19. Lee TW, Robinson JR. Drug delivery to the posterior segment of the eye: some insights on the penetration pathways after subconjunctival injection. J Ocul Pharmacol Ther 2001;17(6):565-572.

20. Oishi M, Maeda S, Hashida N, Ohguro N, Tano Y, Kurokawa N. Pharmacokinetic behavior of intravitreal triamcinolone acetonide prepared by a hospital pharmacy. Jpn J Ophthalmol 2008;52(6):489-492.

21. Berkowitz BA, Roberts R, Luan H, Peysakhov J, Mao X, Thomas KA. Dynamic contrast-enhanced MRI measurements of passive permeability through blood retinal barrier in diabetic rats. Invest Ophthalmol Vis Sci 2004;45(7):2391-2398.

22. Kim H, Robinson MR, Lizak MJ, et al. Controlled drug release from an ocular implant: an evaluation using dynamic three-dimensional magnetic resonance imaging. Invest Ophthalmol Vis Sci 2004;45(8):2722-2731.

23. Friedrich S, Cheng YL, Saville B. Drug distribution in the vitreous humor of the human eye: the effects of intravitreal injection position and volume. Curr Eye Res 1997;16(7):663-669.

24. Friedrich S, Cheng YL, Saville B. Finite element modeling of drug distribution in the vitreous humor of the rabbit eye. Ann Biomed Eng 1997;25(2):303-314.

25. Wiedmann TS, Bhatia R, Wattenberg LW. Drug solubilization in lung surfactant. J Control Release 2000;65(1-2):43-47.

26. Yang CS, Khawly JA, Hainsworth DP, et al. An intravitreal sustained-release triamcinolone and 5-fluorouracil codrug in the treatment of experimental proliferative vitreoretinopathy. Arch Ophthalmol 1998;116(1):69-77.

CHAPTER 5

^{19}F-MRI-BASED PHARMACOKINETICS ON A 3T CLINICAL MRI SYSTEM

This chapter is based on the paper "^{19}F-MRI-based pharmacokinetics on a 3T clinical MRI system," which was submitted to the Journal of Magnetic Resonance Imaging in 2011, authored by Xin Liu, Zhong-Xing Jiang, Yihua Bruce Yu and Eun-Kee Jeong.

5.1 Introduction

This traditional population pharmacokinetic (PK) study requires sacrificing a large number of animals at various time points. The organs are extracted, and the concentration of the drug in the organs is then determined *in vitro*, using assays such as high-performance liquid chromatography (HPLC). Such a PK study is based on the assumption that all the animals sacrificed at different time points have the same biological conditions. The degree to which this assumption is violated may introduce considerable variance in the PK parameters extracted from the data.

For *in vivo* experiments, only plasma or excreted drug concentration is normally accessible, but not tissue concentration. Plasma levels of compounds often differ from concentrations in specific tissues. The drug

concentrations can be either higher or lower in the tissue compared to the plasma (1).

MRI provides a noninvasive means to trace drug distribution *in vivo*. Dynamic-Contrast-Enhanced MRI (DCE MRI) with a paramagnetic contrast agent is commonly used to study pharmacokinetics (2-3). Paramagnetic ions can reduce the spin-lattice relaxation time (T_1) of water proton NMR; as a result, T_1-weighted images show enhanced signal intensities in the vicinity of paramagnetic ions. The higher the local concentration of paramagnetic ions, the larger the enhancement of the signal intensity. The signal intensity of NMR varies nonlinearly with the concentration of the contrast agent, according to the equations:

$$S(C) = S_0\left(1 - e^{-\frac{TR}{T_{1(C)}}}\right)e^{-\frac{TE}{T_{2(C)}}} \quad \ldots.(5.1)$$

$$\frac{1}{T_1(C)} = \frac{1}{T_{10}} + r_1 \times C \quad \ldots.(5.2)$$

$$\frac{1}{T_2(C)} = \frac{1}{T_{20}} + r_2 \times C \quad \ldots.(5.3)$$

Here, $S(C)$ is the enhanced signal intensity, S_0 is the thermal equilibrium signal intensity, TR is the recovery time, TE is the echo time, $T_1(C)$ and $T_2(C)$ are the concentration-dependent spin-lattice and spin-spin relaxation times, respectively, T_{10} is the spin-lattice relaxation time with no contrast agent, T_{20} the spin-spin relaxation time with no contrast agent, C is the contrast agent

concentration, and r_1 and r_2 are the relaxivities of the contrast agent. At very low concentration, the signal intensity is approximately a linear function of the concentration of the contrast agent. Although the large concentration (about 88 M) of water protons provides great sensitivity for anatomical proton MR images, it also presents a potentially confounding and ubiquitous background signal in detecting the tracking agent, particularly if the latter is present at a much lower concentration.

Nonproton MRI has rarely been used to study pharmacokinetics, because its signal intensity is generally low. Although hyperpolarized gas (^{3}He or ^{129}Xe) MRI can provide high signal intensity, and therefore high temporal resolution, the short life time (about 30 sec) of *in vivo* hyperpolarized gas limits the observation window. Also because the same flipangle is generally used at each time point, magnetization tipped to the transverse plane to generate the signal varies from one time point to another, making it hard to quantify tracer concentration over different time points. ^{19}F MR has its advantages, although its signal intensity cannot be compared to hyperpolarized gas. It has a high gyromagnetic ratio compared to other non-proton nuclei, no background signal, 100% abundance, and reusable magnetization (unlike hyperpolarized magnetization). ^{19}F MR imaging and spectroscopy have been used to study a variety of biologic processes including metabolism (4-6), tumor growth (7-9), blood flow (10-11) and cell tracking (12). However, most fluorinated compounds are not for *in vivo* ^{19}F MRI

applications because of their low-intensity signals, complex peak shapes that result in further signal loss, long T_1, and long retention time *in vivo* due to low hydrophilicity or water solubility. ^{19}F MR spectroscopy (MRS) has been used to investigate the clearance of the corticosteroid drug (triamcinolone acetonide phosphate) in the eye (13), delivery of psychiatric drugs, e.g., trifluorinated neuroleptics (fluphenazine and trifluoperazine) and trifluorinated antidepressants (fluoxetine and fluvoxamine) (14) and anticancer drugs, e.g., 5-FU (15-16). There are some ^{19}F MR imaging studies on high field magnets (17-19) or using an extended acquisition time (20). In this paper, we present fluorine MR imaging with a newly developed fluorine compound, ^{19}FIT (^{19}F imaging tracer), which has 27 identical fluorine atoms with the same chemical shift, a relatively short T_1, and high hydrophilicity (21).

5.2 Materials and Methods

5.2.1 Drug Preparations

The ^{19}FIT was efficiently synthesized in 11 synthetic steps on a scale of 2-grams with a good yield (21-22). From commercially available starting material pentaerythritol and perfluoro-tert-butanol, the Mitsunobu reaction was employed as a key reaction to introduce 3 symmetrically-positioned trifluoro-tert-butyl groups. Then, ^{19}FIT was synthesized in a sequential manner using repetitive deprotection/condensation cycles. Since most of the intermediates contain 27 fluorine atoms, those intermediates were easily

purified utilizing the unique separation power of fluorous chemistry. The final product ^{19}FIT was purified using a combination of fluorous silica-gel chromatography and preparative HPLC. Molecular weight and purity of the final product were verified by mass spectrometry and analytical HPLC, respectively.

5.2.2 Animal Experiments

BALB/C male white mice 60 - 80 days old were purchased from Charles River Laboratories International Inc. (Wilmington, MA). The animal experiment protocol was approved by the Institutional Animal Care and Use Committee at the University of Utah. Healthy mice were anesthetized by intramuscular injection of 100 mg/kg Ketamine and 5~10 mg/kg Xylazine. Two mice received 400 µl 150 mM ^{19}FIT (2.2 mmol/kg ^{19}FIT concentration, 60 mmol/kg ^{19}F concentration) and two mice received 200 µl saline and 200 µl 150 mM ^{19}FIT (1.1 mmol/kg ^{19}FIT concentration, 30 mmol/kg ^{19}F concentration) through the tail vein. During the MRI scan, the mice were placed on a mouse bed inside the imaging coil in a prone position. ^{19}F images were obtained at different time points, and *^{1}H images were acquired* at the same location immediately after taking the ^{19}F images.

5.2.3 MRI Experiments

All MRI experiments were performed on a clinical whole body 3T MRI system (Tim-Trio, Siemens Medical Solution, Erlangen, Germany) using a home-built ^{1}H/^{19}F dual-tuned volume coil with 2″ diameter and 3″ length for

RF transmission and signal reception. A coil-to-system interface was constructed. Because the separation between two channels is only 7 MHz at 3.0 T, the coil assembly consists of two separate channels. ^{19}F and ^{1}H channels of the coil were saddle-type coils, which are geometrically oriented at 90° to each other. The interface consists of a PIN-diode driven transmit/receive (T/R) switch, a broadband preamplifier (5 - 200 MHz), a coil-selector switch with coil-code resistors, and a connector. The isolation between the receive and the transmit ports of the T/R switch was about -40 dB when the PIN diode was driven.

^{1}H images were acquired using a 3D gradient echo (GRE) pulse sequence with 0.4×0.4×0.4 mm^3 spatial resolution, 100×50 mm^2 FOV, 7.73 ms TR, 2.74 ms TE, 25° flipangle, 150 Hz/pixel bandwidth, 2 averages and 1 min 11 sec imaging time. ^{19}F images were obtained at the same location by a 2D GRE pulse sequence with 1.5×1.5×3.0 mm^3 spatial resolution, 192×96 mm^2 FOV, 400 ms TR, 2.98 ms TE, 90° flipangle, 260 Hz/pixel bandwidth, 16 averages and 5 min 9 sec imaging time, 75 % asymmetric phase-encoding was used. All MR images were taken on the coronal plane. To assess the total fluorine amount, whole-body spectra were acquired using an FID pulse sequence with 8 averages, 100 kHz bandwidth, 0.15 ms TE and 1.6 sec TR. *In vivo* T_1 of ^{19}FIT was also measured using a series of whole body FID signals with recovery times of 0.2, 0.4, 0.8, 1.6, and 3.2 sec.

5.2.4 MR Data Processing

All ^{19}F spectra were processed using MR spectroscopy analysis software developed in our lab using IDL (Interactive Data Language, ITT Visual Software, Boulder, CO). The data were apodized with 10 Hz Gaussian line broadening, Fourier-transformed, and phase-corrected. The signal intensities of the whole-body FIDs were fit to an exponential recovery curve to extract T_1.

5.3 Results

5.3.1 ^{19}F Spectra

A typical fluorine spectrum obtained 2 days after the injection from one mouse, which received 2.2 mmol/kg ^{19}FIT, is shown in Fig. 5.1. There is no fluorine peak other than the one from ^{19}FIT within 100kHz bandwidth. No other peak was observed at different time points or from different mice, which indicates that all fluorine nuclei in ^{19}FIT have an identical chemical environment *in vivo*. MR spectroscopy and HPLC analysis were also done on the urine samples collected from the mice that received ^{19}FIT. There was no sign of the degradation of ^{19}FIT *in vivo*, as reported in our previous paper (21). The average of whole body fluorine FID signals were taken from two mice (which received 2.2 mmol/kg ^{19}FIT) at a series of time points. The data points were fitted to the function $S=S_0+A\times\exp(-t/\tau)$, and the elimination time constant τ was calculated as 1030.0±55.3 min. For the two mice that received

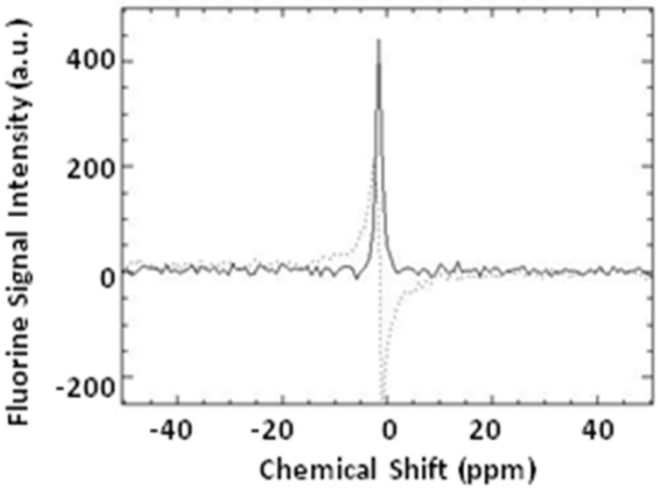

Figure 5.1. An *in vivo* whole body fluorine spectrum of one mouse which received 2.2 mmol/kg ^{19}FIT, taken 2 days after the injection.

1.1 mmol/kg ^{19}FIT, the elimination time constant τ is 1154.1±344.8 min, as we reported in our previous paper (21).

After 2 days, whole-body signal intensities dropped down to one tenth from the initial signal intensity for both mice; 6 days later residual signals were 1/26 and 1/20 of the original amount for 2.2 mmol/kg and 1.1 mmol/kg doses, respectively. In other words, after 6 days, the total detectable ^{19}F compounds were 0.085 mmol/kg and 0.055 mmol/kg for initial dosages of 2.2 mmol/kg and 1.1 mmol/kg, respectively.

5.3.2 Pharmacokinetics by ^{19}F Imaging

Fig.5.2 shows the ^{19}F images of one mouse that received 2.2 mmol/kg of ^{19}FIT, at different time points and slices after the injection. Because of the lack of ^{19}F background MR signal *in vivo*, the hyperintensities on the ^{19}F images are derived only from the ^{19}FIT signal. The SNR of these fluorine images at early time points around the heart and liver regions range from 5 to 10. At later time points, when most of the ^{19}FIT has accumulated in the bladder, the SNR around the bladder region is 30-40.

For the mouse shown in Fig 5.2, at each time point, the fluorine signal in a given organ is obtained by summing over all the slices in that organ. The changes in the total fluorine signals over time from the different organs are plotted in Fig. 5.3a, the rapid fluorine signal drop in heart and liver, and dramatic increase in bladder signal during the first few hours can be quantitatively observed. The fluorine signals in the other mouse that received

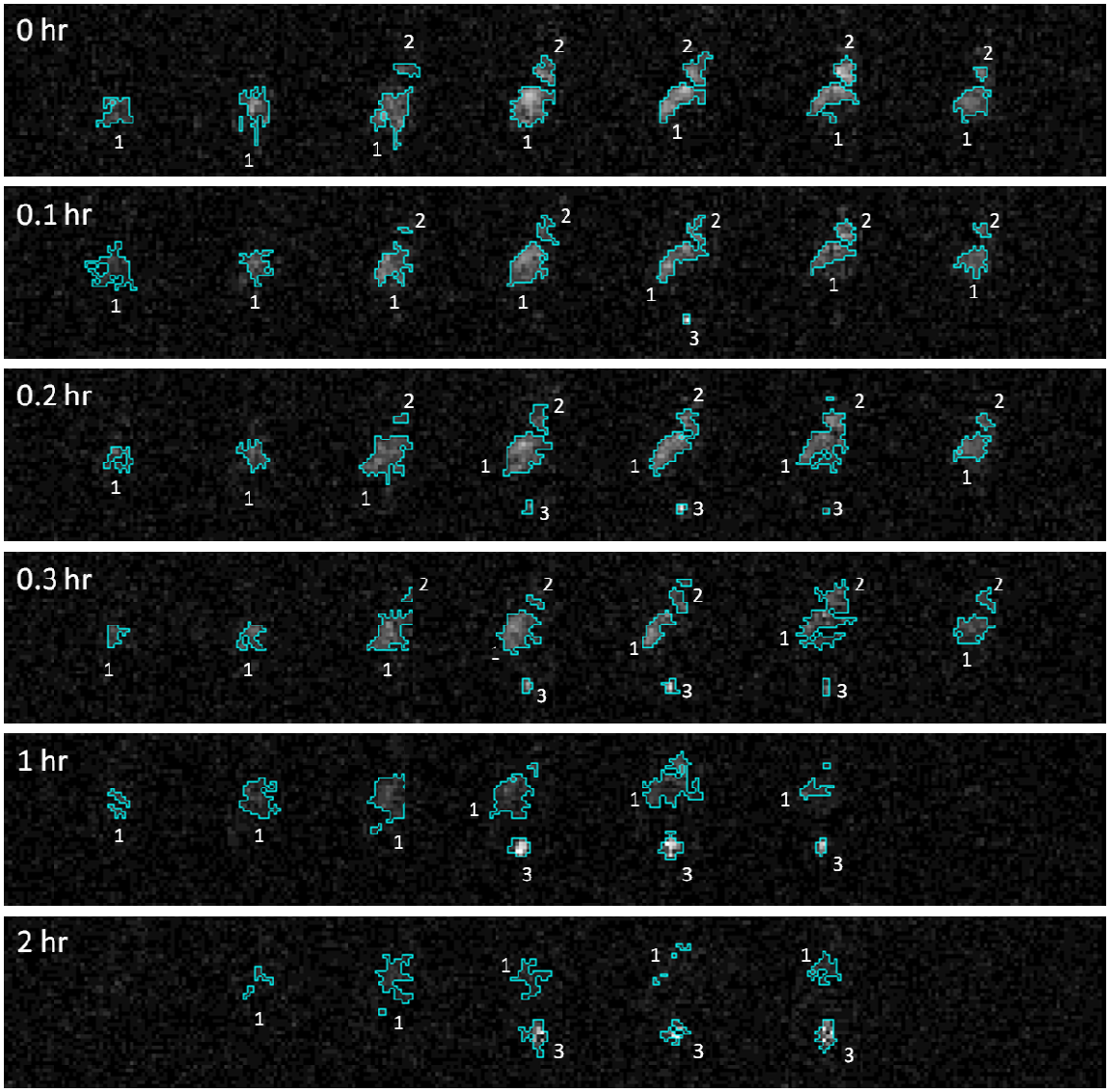

Figure 5.2. The fluorine images from a mouse with dosage of 2.2 mmol/kg at the different time points and different slices, the images show how the signal intensity and distribution evolve through time in different organs. In the images, 1, 2 and 3 indicate signals from liver, heart and bladder, respectively.

the 2.2 mmol/kg ^{19}FIT dose and the two mice that received 1.1 mmol/kg ^{19}FIT dose show a similar pattern and are plotted in Fig. 5.3b, c and d. The maximum concentration (C_{max}) and area-under-curve (AUC) have been calculated using the organ fluorine signal curves, and are listed in Table 5.1.

The T_1 of the ^{19}FIT solution in vial was 253.3±25.0 ms and *in vivo* T_1 of ^{19}FIT from one mouse with 1.1 mmol/kg ^{19}FIT was 393.1±48.0 ms, 368.2±5.9 ms, 420.9±83.8 ms and 314.3±52.8 ms for times 0, 4 hours, 8 hours and 24 hours after the injection. The prolonged T_1 of ^{19}FIT *in vivo* is possibly caused by the hindered molecular rotational motion of the compound *in vivo* and needs to be further investigated.

To extract more information from specific organs, three regions of interest (ROI) were selected from the slice of the mouse shown in Fig. 5.2. The three ROIs are in the heart, liver and bladder, respectively. All the ROIs were chosen to have the same area. The mean value of the fluorine signals of each pixel inside the ROI was calculated for each time point. The time change curves are shown in Fig. 5.4. At the 2-hour time point, the signals from heart and liver ROIs are undetectable. Compared to the total organ signals shown in Fig. 5.3, the signal in the liver can still be detected at the 4-hour time point. This indicates that different regions of the same organ (e.g., liver) have different uptake process and clearance rate.

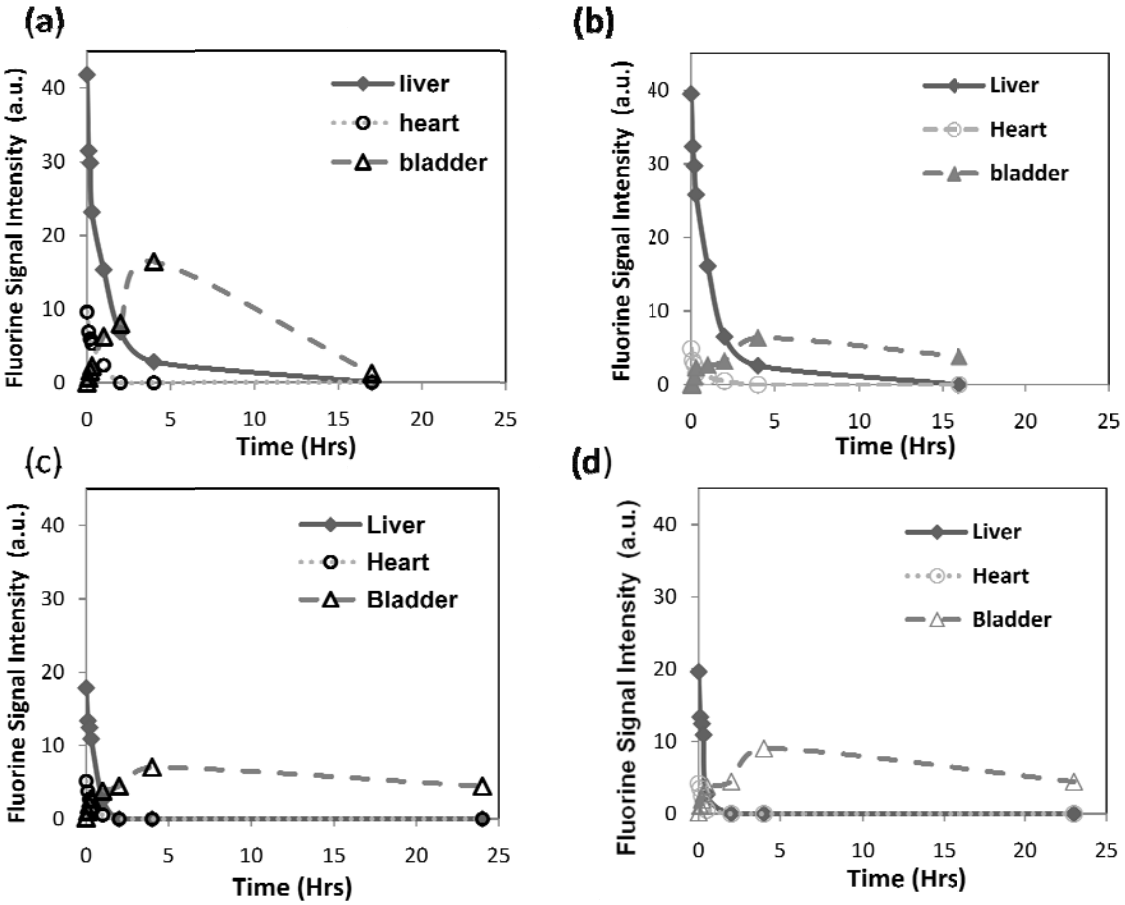

Figure 5.3. Fluorine signal from liver, heart or bladder was summed over all the slices at each time point; the summations yield the total signal from the organs at each time. The dynamic total fluorine signal for each organ is shown in the figure. (a) and (b) are from two mice that received 2.2 mmole/kg ^{19}FIT , (c)and (d) are from two mice that received 1.1 mmole/kg ^{19}FIT.

Table 5.1. M1, M2 indicate the two mice that received 2.2 mmol/kg ^{19}FIT and M3, M4 indicate the two mice that received 1.1 mmol/kg ^{19}FIT. The ^{19}FIT concentrations were converted from fluorine signal with arbitrary unit.

	C_{max}(a.u.)	AUC (a.u.×hr)
Liver (M1)	41.8	62.4
Heart (M1)	9.6	5.9
Bladder (M1)	16.4	149.6
Liver (M2)	59.5	90.3
Heart (M2)	7.3	4.6
Bladder (M2)	9.5	112.9
Liver (M3)	17.9	10.1
Heart (M3)	5.2	1.9
Bladder (M3)	7.0	133.3
Liver (M4)	19.7	7.5
Heart (M4)	4.1	1.5
Bladder (M4)	9.0	148.1

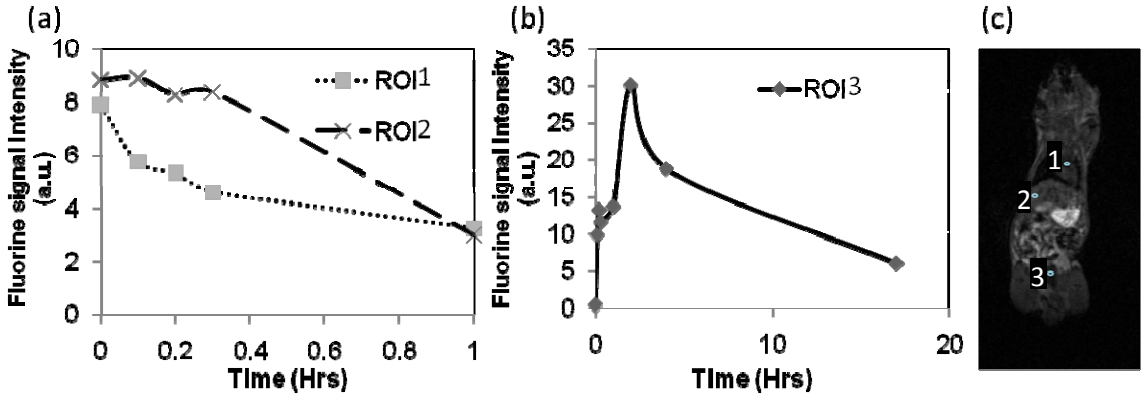

Figure 5.4. The dynamic fluorine signal from 3 ROIs are shown in the Figures. ROI 1, 2 and 3 are selected from the heart region, liver region and bladder region, respectively, in a center slice of a mouse that received 2.2 mmol/kg ^{19}FIT, 3 ROIs are indicated in the ^{1}H anatomy image on the right.

5.4 Discussion

MRI is a powerful tool for studying drug distribution or metabolism *in vivo in situ*. ^{19}F MRI of a fluorinated substance with a large number of chemically identical ^{19}F nuclei has several advantages over a gadolinium-based contrast agent, including the absence of background ^{19}F NMR signal in biological tissue and direct observation of the imaging agent. The signal intensity of density-weighted ^{19}F MRI is linear with the local concentration of the compound in the imaging voxel, unlike the nonlinear relationship between the ^{1}H MRI signal intensity and the gadolinium-based contrast agent concentration. In this study, we tracked real time ^{19}F pharmacokinetics quantitatively on a 3T clinical scanner with a reasonable time resolution (5 min 9 sec). It is probable that this method could be used in human studies in the future because, unlike other methods, which use very long acquisition times that patients cannot tolerate, or high-field MRI systems (such as 7T or 9.4 T) not currently available in clinics – it can be used on commonly-available clinical scanners in reasonable imaging times.

5.4.1 Pharmacokinetics Study of ^{19}FIT

The time curves for signal change in the various organs indicate the clearance pathway of intravenous ^{19}FIT in mouse: ^{19}FIT will go through heart and liver, then accumulate in the bladder and be excreted via urine (21). Because the ^{19}F imaging resolution is considerably low, there is a partial volume effect when we calculate the signals from the heart and liver,

especially at some early time points when the signals in the liver and heart are connected together, as shown in Fig.5.2.

The ROI signal curve can reveal more information about the compound dynamics inside each organ, to study the function of the organs. Since the mice were moved from one time point to another (except the first few points, which were obtained with the animal in the same position), there might be some misregistration problems for each ROI, although we tried to keep the mice in the same posture and position.

Because of the linear relationship between fluorine signal and actual compound amount, fluorine signal change can be used to show the maximum uptake of the drug, which in some cases is information that can modify the therapy. Organ concentration can be used to extract PK parameters combined with plasma concentration using PK models. To obtain absolute quantification, we can put an external phantom with a known concentration of fluorine nuclei next to the subject and use the phantom signal as a reference to estimate the ^{19}FIT level *in vivo*, as reported (23).

From the *in vivo* ^{19}F spectrum, since there is no other peak appearing within the 100 kHz bandwidth centered at the frequency of ^{19}FIT, there is no breakdown of ^{19}FIT *in vivo* or binding between ^{19}FIT and tissue to affect the chemical shift of ^{19}FIT. The whole body spectra can be used to monitor the total amount of ^{19}FIT left inside the body, from which parameters such as elimination rate of the drug can be obtained.

5.4.2 Further Improvement of Fluorine Imaging

Although the doses of ^{19}FIT used in our experiments (1.1 and 2.2 mmol/kg) are very high compared with clinical dose Gd-based contrast agents, e.g. 0.1 mmol/kg, no acute toxicity or weight loss was observed within 45 days after the injection, as reported in our previous paper (21). The dose can be reduced by conjugating an increased number of fluorine atoms in each ^{19}FIT molecule.

Currently the ^{19}F imaging protocol is not optimized. Because of the relative long *in vivo* T1 (~300-400 ms) compared to TR, the 400 ms TR and 90º flipangle make the fluorine imaging not only fluorine density weighted, but T_1 dependent. This will make quantification more complicated. Since these are preliminary results, and the T_1 of the compound can be shortened, which is discussed below, the results still show the feasibility of the dynamic fluorine imaging of ^{19}FIT.

One way to further improve SNR of ^{19}F MRI is to add more fluorine atoms in each molecule. The shortcoming is the higher hydrophobicity with more fluorine atoms which will increase the retention time of the compound. Another way is to reduce T_1 of the compound. There are reports about using paramagnetic ion, e.g., Gd, to trim the relaxation times (T_1 and T_2) of the fluorine spin of fluorine compounds (24-25). With T_1 shortened by nearby paramagnetic ions, the repetition time (TR) can be significantly reduced. The reduced TR can either be used to shorten imaging times, or traded for an

increase in the number of repetitions in the same time period, thereby increasing SNR.

To increase the sensitivity of ^{19}F imaging for human applications, it is possible to use a surface coil placed near the target organ. The drawback to this is very non-uniform sensitivity within the coil detection region, which leads to difficulties in quantification.

5.5 Conclusions

Whole-body dynamic fluorine imaging of a newly developed fluorine imaging agent, ^{19}FIT, in mice is reported with fairly high spatial resolution and temporal resolution on a 3T clinical MRI scanner. The biodistribution and pharmacokinetics of ^{19}FIT are obtained via ^{19}F images for major uptake organs. The present study demonstrates the feasibility of using ^{19}F MRI to investigate pharmacokinetics.

5.6 Acknowledgements

This work was partly supported by a VP Seed Grant of the University of Utah, the Ben B. and Iris M. Margolis Foundation, and NIH Grants EY15181 and EB004416. The authors want to thank Dr. June Taylor for helpful discussions.

5.7 References

1. Reid DG, Murphy PS. Fluorine magnetic resonance in vivo: a powerful tool in the study of drug distribution and metabolism. Drug Discov Today 2008;13(11-12):473-480.

2. Kim SH, Csaky KG, Wang NS, Lutz RJ. Drug elimination kinetics following subconjunctival injection using dynamic contrast-enhanced magnetic resonance imaging. Pharm Res 2008;25(3):512-520.

3. Wang Y, Ye F, Jeong EK, Sun Y, Parker DL, Lu ZR. Noninvasive visualization of pharmacokinetics, biodistribution and tumor targeting of poly[N-(2-hydroxypropyl)methacrylamide] in mice using contrast enhanced MRI. Pharm Res 2007;24(6):1208-1216.

4. Klomp D, van Laarhoven H, Scheenen T, Kamm Y, Heerschap A. Quantitative 19F MR spectroscopy at 3 T to detect heterogeneous capecitabine metabolism in human liver. NMR Biomed 2007;20(5):485-492.

5. Schneider E, Bolo NR, Frederick B, et al. Magnetic resonance spectroscopy for measuring the biodistribution and in situ in vivo pharmacokinetics of fluorinated compounds: validation using an investigation of liver and heart disposition of tecastemizole. J Clin Pharm Ther 2006;31(3):261-273.

6. van Laarhoven HW, Punt CJ, Kamm YJ, Heerschap A. Monitoring fluoropyrimidine metabolism in solid tumors with in vivo (19)F magnetic resonance spectroscopy. Crit Rev Oncol Hematol 2005;56(3):321-343.

7. Porcari P, Capuani S, D'Amore E, et al. In vivo 19F MR imaging and spectroscopy for the BNCT optimization. Appl Radiat Isot 2009;67(7-8 Suppl):S365-368.

8. Procissi D, Claus F, Burgman P, et al. In vivo 19F magnetic resonance spectroscopy and chemical shift imaging of tri-fluoro-nitroimidazole as a potential hypoxia reporter in solid tumors. Clin Cancer Res 2007;13(12):3738-3747.

9. Ramaprasad S, Ripp E, Missert J, Pandey RK. In vivo 19F MR studies of fluorine labeled photosensitizers in a murine tumor model. Curr Drug Discov Technol 2007;4(2):126-132.

10. Ligeti L, Pekar J, Ruttner Z, McLaughlin AC. Determination of cerebral oxygen consumption and blood flow by magnetic resonance imaging. Acta Biomed Ateneo Parmense 1995;66(3-4):67-74.

11. van Zijl PC, Ligeti L, Sinnwell T, et al. Measurement of cerebral blood flow by volume-selective 19F NMR spectroscopy. Magn Reson Med 1990;16(3):489-495.

12. Janjic JM, Ahrens ET. Fluorine-containing nanoemulsions for MRI cell tracking. Wiley Interdiscip Rev Nanomed Nanobiotechnol 2009;1(5):492-501.

13. Liu X, Kevin Li S, Jeong EK. Ocular pharmacokinetic study of a corticosteroid by 19F MR. Exp Eye Res 2010;91(3):347-352.

14. Bartels M, Albert K. Detection of psychoactive drugs using 19F MR spectroscopy. J Neural Transm Gen Sect 1995;99(1-3):1-6.

15. Kamm YJ, Heerschap A, van den Bergh EJ, Wagener DJ. 19F-magnetic resonance spectroscopy in patients with liver metastases of colorectal cancer treated with 5-fluorouracil. Anticancer Drugs 2004;15(3):229-233.

16. Dresselaers T, Theys J, Nuyts S, et al. Non-invasive 19F MR spectroscopy of 5-fluorocytosine to 5-fluorouracil conversion by recombinant Salmonella in tumours. Br J Cancer 2003;89(9):1796-1801.

17. Kimura A, Narazaki M, Kanazawa Y, Fujiwara H. 19F Magnetic resonance imaging of perfluorooctanoic acid encapsulated in liposome for biodistribution measurement. Magn Reson Imaging 2004;22(6):855-860.

18. Bolo NR, Hode Y, Nedelec JF, Laine E, Wagner G, Macher JP. Brain pharmacokinetics and tissue distribution in vivo of fluvoxamine and fluoxetine by fluorine magnetic resonance spectroscopy. Neuropsychopharmacology 2000;23(4):428-438.

19. Doi Y, Shimmura T, Kuribayashi H, Tanaka Y, Kanazawa Y. Quantitative (19)F imaging of nmol-level F-nucleotides/-sides from 5-FU with T(2) mapping in mice at 9.4T. Magn Reson Med 2009;62(5):1129-1139.

20. Brix G, Schlicker A, Mier W, Peschke P, Bellemann ME. Biodistribution and pharmacokinetics of the (19)F-labeled radiosensitizer 3-aminobenzamide: assessment by (19)F MR imaging. Magn Reson Imaging 2005;23(9):967-976.

21. Jiang ZX, Liu X, Jeong EK, Yu YB. Symmetry-guided design and fluorous synthesis of a stable and rapidly excreted imaging tracer for (19)F MRI. Angew Chem Int Ed Engl 2009;48(26):4755-4758.

22. Jiang ZX, Yu YB. Fluorous mixture synthesis of asymmetric dendrimers. J Org Chem 2010;75(6):2044-2049.

23. Srinivas M, Morel PA, Ernst LA, Laidlaw DH, Ahrens ET. Fluorine-19 MRI for visualization and quantification of cell migration in a diabetes model. Magn Reson Med 2007;58(4):725-734.

24. Chalmers KH, De Luca E, Hogg NH, et al. Design principles and theory of paramagnetic fluorine-labelled lanthanide complexes as probes for (19)F magnetic resonance: a proof-of-concept study. Chemistry 2010;16(1):134-148.

25. Neubauer AM, Myerson J, Caruthers SD, et al. Gadolinium-modulated 19F signals from perfluorocarbon nanoparticles as a new strategy for molecular imaging. Magn Reson Med 2008;60(5):1066-1072.

CHAPTER 6

CONCLUSION

6.1 Summary

With novel development of more sophisticated and potent drugs, innovative drug delivery systems are required to insure the drug will release at the right time to the right target. It is beneficial to monitor the drug or imaging agent during the delivery process to evaluate the effectiveness of the drug delivery system. MRI provides a noninvasive method to quantitatively assess the *in vivo* pharmaceutical profile.

Currently, MR imaging is conducted on ^{1}H nuclei of the tissue water in clinical MRI, and imaging techniques are well developed and available on every clinical MR systems. Due to the large intrinsic ^{1}H signal in living tissue, to utilize ^{1}H MRI to monitor drug delivery, an imaging contrast agent as imaging tracer is required. GBCA has been widely used clinically as a T_1 relaxation contrast agent. It is necessary to measure the local concentration of GBCA for further quantification of the pharmacokinetics parameters, for instance, blood perfusion and tissue permeability calculation. To make the quantification of GBCA concentration rapid and accurate, a T_1 and T_2 mapping technique ms-DSEPI-T12 was developed and shown in Chapter 3.

ms-DSEPI-T12 greatly improved the temporal resolution of T_1 mapping by utilizing the fact that the thermal magnetization of a pixel remains constant regardless of T_1 shortening. For the current set up, each time point takes only 15 seconds compared to several minutes using conventional imaging methods to measureT_1, such as inversion recovery or saturation recovery. The accuracy of the technique was demonstrated via phantom experiments. The difference in T_1 measurement using ms-DSEPI-T12 and inversion recovery is less than 1%. ms-DSEPI-T12 also shows superiority in insensitivity of B_1 variation to another rapid T_1 mapping technique - fast gradient echo imaging with flipangle variation.

Density-weighted ^{19}F MR imaging and spectroscopy have advantages over ^{1}H MRI for applications in quantitative drug delivery research, because of their linear relationship between the signal intensity and ^{19}F concentration and no background signal interference. An application of ^{19}F MR spectroscopy in ocular pharmacokinetics of corticosteroids is demonstrated in Chapter 4. The conventional methods to study ocular pharmacokinetics use the surgical procedure to extract tissue samples from the eye, and may cause severe complications and the drug concentration can only be estimated. Our study shows that ^{19}F MR is a promising alternative approach that overcomes the major defects of conventional methods.

Although ^{19}F MR is proven beneficial in application to ocular pharmacokinetics, it also reveals one of the common weaknesses of MR ^{19}F

imaging agent, the low signal intensity. Besides the low signal intensity, multiple chemical shifts, long T_1 and long retention time of the perfluorocarbon (PFC) that are most commonly used for ^{19}F MRI, prevent themselves from being suitable MR ^{19}F imaging agents. Lack of desired imaging agents has hindered the applications of ^{19}F MRI. A newly developed MR ^{19}F imaging agent greatly overcomes these shortcomings, and the ^{19}F MRI based pharmacokinetic study has been done in Chapter 5. Relatively higher SNR of the ^{19}F dynamic images are obtained on a 3T clinical system.

6.2 Limitations and Perspectives

Current ms-DSEPI-T12 technique (temporal resolution 15 sec) is not fast enough to measure the arterial input function (AIF) to calculate pharmacokinetic parameters such as tissue permeability, which requires temporal resolution on one second order. To further boost the speed of the dynamic measurement, (1) a sliding window technique can be used, and (2) a larger echo train length might be helpful, although it induces increased geometric distortion due to variations in the local magnetic field because of the magnetic susceptibility. If the temporal resolution is still not high enough, then we have to adopt an AIF free model, e.g., reference region model.

For ^{19}F MR ocular pharmacokinetics project, DSP as a widely used corticosteroid in the treatment might be chosen as a role model in future studies. Because the clinical dosage of DSP is approximately 10 times less than that used in our TAP study, further improvement of the hardware is

required to increase the signal intensity. If the DSP sensitivity can exceed the detection limit, the technique might eventually be applied to humans.

To improve the SNR or temporal resolution of ^{19}FIT imaging, modifications to ^{19}FIT can be done via (1) adding more fluorine atoms into the molecule, although it can reduce the hydrophilicity, and (2) utilizing a paramagnetic ion attached to ^{19}FIT to reduce its T_1 relaxation time. Besides, imaging sequence and sequence parameters can be more optimized.